

# An Intertwined Short and Long GRB with 4-minute Separation

Liang Li<sup>1,2\*</sup>, Yu Wang<sup>3,4,5†</sup>, Bing Zhang<sup>6,7,8\*</sup>, Ye Li<sup>9</sup>, Shu-Rui Zhang<sup>10</sup>, Jochen Greiner<sup>11</sup>, Zhi-Ping Jin<sup>7</sup>, Jin-Jun Geng<sup>7</sup>, Hou-Jun Lü<sup>12</sup>, Asaf Pe'er<sup>13</sup>, Maria Dainotti<sup>14</sup>, Tong Liu<sup>15</sup>, Yi-Zhong Fan<sup>7</sup>, Yong-Feng Huang<sup>16,17</sup>, Zi-Gao Dai<sup>10</sup>, Melin Kole<sup>16,17</sup>, Wei-Hua Lei<sup>20</sup>, Ye-Fei Yuan<sup>10</sup>, Shuang-Nan Zhang<sup>21</sup>, Felix Ryde<sup>22</sup>, She-Sheng Xue<sup>3,4</sup>, Rong-Gen Cai<sup>1\*</sup>

<sup>1</sup>Institute of Fundamental Physics and Quantum Technology, Ningbo University, Ningbo, Zhejiang 315211, China.

<sup>2</sup>Department of Physics, School of Physical Science and Technology, Ningbo University, Ningbo, Zhejiang 315211, China.

<sup>3</sup>Dip. di Fisica and ICRA, Sapienza Università di Roma, Piazzale Aldo Moro 5, I-00185 Rome, Italy.

<sup>4</sup>ICRANet, Piazza della Repubblica 10, 65122 Pescara, Italy.

<sup>5</sup>INAF – Osservatorio Astronomico d’Abruzzo, Via M. Maggini snc, I-64100, Teramo, Italy.

<sup>6</sup>The Hong Long Institute for Astronomy and Astrophysics, University of Hong Kong, Pokfulam Road, Hong Kong, China.

<sup>7</sup>Department of Physics, University of Hong Kong, Pokfulam Road, Hong Kong, China.

<sup>8</sup>Department of Physics and Astronomy, University of Nevada, Las Vegas, NV 89154, USA.

<sup>9</sup>Purple Mountain Observatory, Chinese Academy of Sciences, Nanjing 210023, China.

<sup>10</sup>Department of Astronomy, University of Science and Technology of China, Hefei 230026, China.

<sup>11</sup>Max-Planck Institut für extraterrestrische Physik, Giessenbachstr. 1, 85748 Garching, Germany.

<sup>12</sup>Guangxi Key Laboratory for Relativistic Astrophysics, School of Physical Science and Technology, Guangxi University, Nanning, 530004, China.

<sup>13</sup>Department of Physics, Bar-Ilan University, Ramat-Gan 52900, Israel.

<sup>14</sup>Division of Science, National Astronomical Observatory of Japan, 2-21-1 Osawa, Mitaka, Tokyo.

<sup>15</sup>Department of Astronomy, Xiamen University, Xiamen, Fujian 361005, China.

<sup>16</sup>School of Astronomy and Space Science, Nanjing University, Nanjing 210023, China.

<sup>17</sup>Key Laboratory of Modern Astronomy and Astrophysics (Nanjing University), Ministry of Education, China.

<sup>18</sup>University of New Hampshire, Space Science Center, University of New Hampshire, Durham, NH 03824, USA.

<sup>19</sup>Department of Nuclear and Particle Physics, University of Geneva, 24 quai Ernest-Ansermet, 1205 Geneva, Switzerland.

<sup>20</sup>Department of Astronomy, School of Physics, Huazhong University of Science and Technology, Wuhan, Hubei 430074, China.

<sup>21</sup>Key Laboratory of Particle Astrophysics, Institute of High Energy Physics, Chinese Academy of Sciences, Beijing 100049, China.

<sup>22</sup>Department of Physics, KTH Royal Institute of Technology, and The Oskar Klein Centre, SE-10691 Stockholm, Sweden.

\*Email: liliang@nbu.edu.cn (L.L.); yu.wang@inaf.it (Y.W.); zhang@physics.unlv.edu (B.Z.); cairg@itp.ac.cn (R.G.C.)

**Gamma-ray bursts (GRBs), among the most energetic transients in the Universe, are traditionally classified into long-duration GRBs (lasting more than two seconds) and short-duration GRBs (lasting less than two seconds) (1). Long-duration GRBs are typically associated with the core collapse of massive stars (Type II), whereas short-duration GRBs originate from the merger of compact binary systems (Type I) (2–5). Owing to their distinct physical origins, the two classes exhibit markedly different observational properties, which serve as key diagnostic criteria for GRB classification (4, 6–11). Here we report a peculiar gamma-ray burst, GRB 160425A, comprising a short-sharp duration burst ( $G_1$ ) followed by a long-broad duration burst ( $G_2$ ), separated by only four minutes. Strikingly, nearly all standard prompt-emission observational diagnostics, including pulse morphology (12), duration (1), hardness ratio (13, 14), minimum variability timescale (15, 16), spectral properties (17), spectral lag (6, 18–20), and established empirical correlations (the Amati and Norris relations (6, 21)), consistently categorize  $G_1$  as a short-like (Type-I, merger-origin) GRB and  $G_2$  as a long-like (Type-II, collapsar-origin) GRB. The coexistence of merger and collapsar signatures within a single event challenges existing progenitor frameworks, calling for a fundamental re-evaluation of GRB classification schemes and progenitor scenarios.**

On 25 April 2016, at 23:26:11 UT, GRB 160425A alerted the Burst Alert Telescope (BAT; (22)) on board the Neil Gehrels *Swift* Observatory, MASTER II, MPG (2.2m), VLT, MASTER-SAAO, and Skynet PROMPT. The net *Swift*/BAT light curve along with its light curve in different energy bands (15–25 keV  $\sim$  100–350 keV), as detected by BAT, is shown in Figure 1a. Long-term follow-up

observations detected the optical counterpart (22–26) and identified its host galaxy and redshift at  $z = 0.555$  (27). A summary of the timing, spectral properties, and host galaxy information of the burst is listed in Table 1.

### Direct prompt-emission observables

One distinct feature of GRB 160425A is that it comprises two sub-bursts  $G_1$  and  $G_2$ , separated by a quiescent interval exceeding 250 seconds during which no significant emission is detected (Figure 1c). The two sub-bursts appear to be independent, providing a unique opportunity to study GRB classification (Materials and Methods). The first sub-burst,  $G_1$ , is particularly interesting due to its short duration ( $\sim 1.7$  s) and a sharply peaked pulse profile (Figure 1b; Materials and Methods), morphologically resembling a classical short-duration GRB, which raises the question of whether it is related to the second sub-burst,  $G_2$ . We further measure the “amplitude parameter”  $f$  of  $G_1$ , defined as the ratio between the peak flux and the average background flux of a GRB (Materials and Methods). We obtain  $f = 2.13 \pm 0.18$  for  $G_1$ , significantly exceeding the typical range for a disguised short-duration GRB, indicating that  $G_1$  is a genuinely short-duration burst and cannot be the tip-of-iceberg of a long-duration GRB (Figure 1d). The second sub-burst,  $G_2$ , has  $T_{90} \approx 51.2$  s (Figure 1b; Materials and Methods), consistent with a canonical long-duration GRB. The positions of  $G_1$  and  $G_2$  are determined independently and consistent with the same BAT location within positional uncertainties, further supported by the common afterglow/host galaxy association (Materials and Methods), suggesting that both sub-bursts likely originate from the same astrophysical system. Timing and spectral properties of  $G_1$  and  $G_2$  are summarized in Table 2.

To test whether the first sub-burst,  $G_1$ , is related to the second sub-burst,  $G_2$ , we compared both sub-bursts with traditional GRB classification schemes (see Figure 2 and Figure S1; Materials and Methods). Figure 2a shows the standard long/short duration–hardness ratio plane, where hardness ratio is defined as the 25–50 keV and the 15–25 keV counts ratio accumulated over the  $T_{90}$  duration<sup>1</sup> of each sub-burst (Materials and Methods). One can see that  $G_1$  occupies the short-hard region of this diagram, while  $G_2$  falls squarely within the long-soft distribution.

The minimum variability timescale (MVT,  $\Delta t_{\min}$ ) is the shortest observable timescale over which significant flux variations are observed in a GRB and provides an additional discriminator between GRB classes. Based on a Fermi GRB sample (16), the median MVT is 18 ms for short-duration GRBs and 134 ms for long-duration GRBs (Materials and Methods). We measure  $\Delta t_{\min} = 18.5 \pm 3.1$  ms for  $G_1$  and  $\Delta t_{\min} = 550 \pm 32$  ms for  $G_2$  (Figure 2b, and Materials and Methods). These results suggest that  $G_1$  exhibits characteristics consistent with short-duration (Type I) GRBs, while  $G_2$  aligns with the properties of long-duration (Type II) GRBs.

Observations show that short-duration GRBs typically exhibit a negligible “spectral lag” whereas long-duration GRBs are associated with a significant spectral lag (19, 20, 28). We measure the 15–25 keV to 25–50 keV spectral lag for each sub-bursts and find  $38 \pm 39$  ms for  $G_1$  and

<sup>1</sup>During which 90% of the burst fluence was accumulated.

1152±264 ms for  $G_2$  (Figure 2c-e; Materials and Methods). The lag of  $G_1$  is consistent with zero, as expected for a Type I burst, while the highly significant lag of  $G_2$  is characteristic of Type II GRBs. Similar results are also found in the luminosity–lag ( $L_{p,iso} - \tau$ ) plane. Plotting the isotropic peak luminosity of each sub-burst on the Norris relation diagram (6) (Figure S1b), we find that  $G_2$  follows the relation defined by long-duration GRBs, whereas  $G_1$  deviates significantly from it, as expected for short-duration GRBs.

### Derived prompt-emission diagnostics

We perform the spectral analysis of  $G_1$  and  $G_2$ . The spectral peak energy is estimated as  $E_p \gtrsim 500$  keV for  $G_1$  and  $E_p = 57.6 \pm 2.7$  keV for  $G_2$  (Table S1, and Materials and Methods). The corresponding observed fluences are  $(8.6 \pm 1.1) \times 10^{-7}$  erg cm<sup>-2</sup> for  $G_1$  and  $(2.5 \pm 0.3) \times 10^{-6}$  erg cm<sup>-2</sup> for  $G_2$ . At the host-galaxy redshift  $z=0.555$ , ref. (27), the isotropic  $\gamma$ -ray energy ( $E_{\gamma,iso}$ ) of  $G_1$  can be estimated as  $E_{\gamma,iso} \sim (7.2 \pm 0.9) \times 10^{50}$  erg, and that of  $G_2$  as  $E_{\gamma,iso} \sim (2.1 \pm 0.3) \times 10^{51}$  erg. We over-plotted the  $E_{p,z}$ - $E_{\gamma,iso}$  diagram (4, 9, 21), and find that  $G_1$  falls within the short-duration (Type I) locus while  $G_2$  lies in the long-duration (Type II) locus (Figure S1a).

The peculiarity of two sub-bursts observed in GRB 160425A is also reflected in its value of the energy-hardness-duration (EHD) parameter (11),  $EHD = E_{p,i,2} E_{iso,51}^{-0.4} T_{90,i}^{-0.5}$ , where  $E_{p,i,2}$  is the rest frame peak energy  $E_{p,i}$  in units of 100 keV,  $E_{iso,51}$  is the isotropic equivalent energy  $E_{\gamma,iso}$  in units of  $10^{51}$  erg, and  $T_{90,i}$  is the rest-frame duration in units of seconds. Ref. (11) demonstrated that EHD provides the most reliable parameter for the blind Type I and Type II classification, with the two populations divided at  $EHD=2.6$ , with Type I GRBs clustering in the high-EHD region and Type II GRBs in the low-EHD region (Materials and Methods). We obtain  $EHD=9.5$  for  $G_1$  and  $EHD=0.01$  for  $G_2$ , placing  $G_1$  firmly in the Type I region and  $G_2$  firmly in the Type II region of the  $EHD$ - $T_{90,i}$  diagram (Figure S1c).

We extend the classification analysis to the phenomenological parameter  $\varepsilon \equiv E_{\gamma,iso,52} / E_{p,z,2}^{5/3}$ , which has been found to be successful in classifying Type I vs. Type II GRBs (7), where  $E_{\gamma,iso,52}$  is the isotropic equivalent energy in units of  $10^{52}$  erg and  $E_{p,z,2}$  is the cosmological rest-frame spectral peak energy in units of 100 keV. The two GRB classes are nicely clustered in high  $\varepsilon$  ( $\varepsilon > 0.03$ ) and low  $\varepsilon$  ( $\varepsilon < 0.03$ ) regions at the separation line by  $\varepsilon \sim 0.03$  using a GRB sample with known redshift (7) (Materials and Methods). For GRB 160425A, we find that  $\varepsilon$  places  $G_1$  in the low- $\varepsilon$  (Type I) region and  $G_2$  in the high- $\varepsilon$  (Type II) region of the  $\log \varepsilon - \log t_{90,z}$  plane (Figure S1d).

### Uniqueness of GRB 160425A in the peculiar GRB population

GRB 160425A is uniquely distinguished from all previously reported peculiar GRBs by the simultaneous presence of three properties: two genuine prompt-like emission episodes, a  $\sim 256$  s background-consistent quiescent gap, and opposite empirical classifications across the gap ( $G_1$  short-like;  $G_2$  long-like). Continuous-emission outliers (29–37) lack a separated prompt-emission pair altogether, while every previously reported quiescent burst either preserves a common prompt-emission class on both sides of the gap (38–40) or contains a post-gap component better identified

as extended emission (18), a flare (41, 42), or afterglow emission onset (43) (Table 3; Materials and Methods). No known event satisfies all three conditions simultaneously, making GRB 160425A observationally unprecedented in the GRB population.

### **Afterglow, supernova, and host-galaxy constraints**

Long-term follow-up multi-wavelength afterglow observations of the burst were carried out by *Swift* (23) and several ground-based optical telescopes (22, 24–26). In general, short-duration GRBs have lower luminosity than typical long-duration GRBs in X-ray afterglows as observed with the *Swift*-XRT (44–47) (Materials and Methods). Figure S2a shows the luminosity of X-ray afterglow emission as a function of rest-frame time. Coincidentally, GRB 160425A resides in the transitional region between short-duration and long-duration bursts, situated at the lower boundary of the long-burst distribution and the upper boundary of the short-burst distribution.

GRB 160425A differs from the typical GRB population by having an unusually high electron energy fraction ( $\epsilon_e \approx 0.62$  vs. 0.2–0.3), an extreme Lorentz factor ( $\Gamma_0 \sim 950$  vs.  $\sim 250$  for long-duration and  $\sim 420$  for short-duration GRBs), and an exceptionally low circumburst density ( $n_0 \sim 1.6 \times 10^{-3} \text{ cm}^{-3}$  vs.  $\sim 0.3 \text{ cm}^{-3}$ ) (Figure S3, and Materials and Methods).

*Swift* optical U-band data was adopted to identify a possible supernova component. After subtracting the host galaxy’s contribution, the U-band flux at time  $\sim 10^6$  s is faint and highly uncertain, making it insufficient to confirm the existence of a supernova component. This result suggests either no supernova component or a very weak one compared to SN 1998bw. This is consistent with the I-band data from CTIO, which found no obvious change of brightness between 7 and 26 days (48) (Figure S4; Materials and Methods).

### **Why standard interpretations are challenged**

These phenomena have never been observed in a GRB before, challenging the traditional classification scheme of long-duration and short-duration bursts. The peculiar properties of GRB 160425A call for a new interpretation that has not been invoked to explain standard short-duration or long-duration GRBs.

There are four possible ways to interpret this peculiar phenomenon, all of which we will show below to be challenging.

The first possibility is that the two bursts in GRB 160425A originate from distinct host galaxies that happen to coincide in space and time. This scenario suggests that two bursts, each from different host galaxies with different redshifts, were observed in the same spatial region within just a four-minute separation in observed time, with both jets directed towards Earth. The probability of observing two isolated bursts within a 250-second interval from two different galaxies, with a positional accuracy of 1.5 arcminutes using the BAT instrument, is approximately  $1.97 \times 10^{-12}$  (Materials and Methods). Such an extremely low probability underscores that this occurrence would be exceedingly rare.

The second possibility is that the two bursts originated from the same host galaxy but at two

different locations, with  $G_1$  originating from a compact binary merger and  $G_2$  originating from the core collapse of a massive star. The probability of observing two isolated bursts within 250 seconds from the same galaxy is even smaller, approximately  $7.9 \times 10^{-13} - 7.9 \times 10^{-12}$  (Materials and Methods). Again, such an extremely low probability disfavors this scenario.

The third possibility is that this is an extreme case of Type I GRB, with the initial short-duration burst ( $G_1$ ) being followed by a long-duration extended emission (EE) tail ( $G_2$ ) tens (or hundreds) seconds later. However, this interpretation has a few drawbacks. First of all, a prolonged quiescent period of up to four minutes after the emission of  $G_1$  and a much higher fluence, a comparable peak flux, and the presence of a strong single-peak pulse profile of  $G_2$  have never been observed in EE, which strongly disfavors this scenario. One may consider  $G_2$  as a bright X-ray flare following short-duration GRBs (42, 49). However, an X-ray flare of this brightness has never been observed, either (Fig.S2c and d). In fact,  $G_2$  aligns with Type II rather than Type I in the  $L_{x,p} - t_{p,z}$  diagram of X-ray flares (Fig.S2e; Materials and Methods). Moreover, the Type I interpretation suffers from additional criticisms. The offset between the GRB location and its host galaxy is calculated to be 1.86 kpc, corresponding to a normalized offset value of 0.7 (Table 1; Materials and Methods). Such a small offset is peculiar for Type I GRBs, but aligns more with Type II GRBs with a massive star core-collapse origin.

This left us with the fourth interpretation, i.e. this is a peculiar Type II GRB with  $G_2$  being the main burst, but with an initial short-duration precursor emission ( $G_1$ ). Such a scenario could be supported if the putative supernova is confirmed, but it is hardly identified. This scenario also suffers from several drawbacks. Typically, the peak flux of a precursor emission is much lower than that of the main emission of a long-duration burst (50, 51). However, in GRB 160425A, the peak flux of  $G_1$  is even higher than that of  $G_2$ . Moreover, the analysis of the  $f$ -value supports  $G_1$  being a genuine short-duration burst rather than a precursor emission of a long-duration burst. More importantly, previous studies (34, 50, 52–56, 56, 57) indicate that these emission components-precursors, prompt gamma-ray emission, and extended soft gamma-ray emission-are likely to share a common physical origin, attributed to the repeated activation of the GRB central engine. Consequently, these distinct components within an individual burst typically exhibit similarities in observational properties, such as spectral lags. This is also in contrast with the observations. Physically, a quiescent gap may be produced if the Type II GRB central engine is intermittent, as shown in numerical simulations of intermittent jets propagating in a massive star envelope (58). However, such a process usually produces weak precursors. The origin of an extremely narrow and hard precursor such as  $G_1$  is still mysterious.

### **Implications**

In conclusion, direct prompt-emission observables (duration, amplitude parameter, hardness ratio, MVT, and spectral lag) already robustly establish a clear contrast between  $G_1$  and  $G_2$ , placing them in the short-like and long-like regimes, respectively. Additional prompt-emission diagnostics

based on derived spectral quantities (Amati and Norris relations, EHD, and  $\varepsilon$  parameters) are consistent with this picture, while afterglow, supernova, and host-galaxy data provide contextual support for this interpretation. Taken together, GRB 160425A is neither a classical short-duration burst ( $G_1$ ) with a later-time soft extended emission component or X-ray flare ( $G_2$ ), nor a typical long-duration burst ( $G_2$ ) preceded by an early-time precursor ( $G_1$ ). Instead, it is most naturally interpreted as an independent short-duration GRB ( $G_1$ ) followed by an independent long-duration GRB ( $G_2$ ) within the same event. The unique properties observed in GRB 160425A provide compelling evidence for a solid transition from a short-like (Type I, merger-origin) to a long-like (Type II, collapsar-origin) episode within a single system. As such, GRB 160425A challenges the traditional morphological classification scheme and our physical understanding of known GRB progenitor types, implying that short-duration and long-duration gamma-ray bursts can occur almost simultaneously within the same astrophysical system, a phenomenon that has been neither observed nor predicted by current theoretical models.

**Table 1:** Properties of GRB 160425A.

<b>Basic Observation</b>	
Duration (15-350 keV) [ $T_{90}$ ]	$304.6 \pm 15.0$ (s)
1-s peak flux (15-150 keV) [ $F_p$ ]	$(2.8 \pm 0.2)$ ( $\text{ph cm}^{-2} \text{s}^{-1}$ )
Peak luminosity (15-150 keV) [ $L_{\gamma, \text{iso}}$ ]	$(2.6 \pm 1.2) \times 10^{50}$ ( $\text{erg s}^{-1}$ )
Total BAT fluence (15-150 keV) [ $S_{\gamma}^{\text{BAT}}$ ]	$(2.1_{-0.2}^{+0.2}) \times 10^{-6}$ ( $\text{erg cm}^{-2}$ )
Total bolometric fluence (1- $10^4$ keV) [ $S_{\gamma}$ ]	$(3.4 \pm 0.3) \times 10^{-6}$ ( $\text{erg cm}^{-2}$ )
Total isotropic energy (1- $10^4$ keV) [ $E_{\gamma, \text{iso}}$ ]	$(4.7_{-2.4}^{+0.7}) \times 10^{51}$ (erg)
Observed frame quiescent gap [ $t_{\text{gap}}$ ]	$255.5_{-9.7}^{+9.3}$ (s)
Rest frame quiescent gap [ $t_{\text{gap}}/(1+z)$ ]	$164.3_{-6.2}^{+6.0}$ (s)
<b>Host Galaxy</b>	
Redshift [ $z$ ]	0.555
Luminosity distance [ $D_L$ ]	3308 (Mpc)
Offset [ $R_{\text{off}}$ ]	1.86 (kpc)
Half light radius [ $R_{50}$ ]	2.5 (kpc)
Normalized offset [ $r_{\text{off}} \equiv R_{\text{off}}/R_{50}$ ]	0.7
Cumulative light fraction [ $F_{\text{light}}$ ]	$\sim 0.6$
Star formation rate [SFR]	$0.58 (M_{\odot} \text{ yr}^{-1})$
Optical transient location	18h 41m 18s $-54^{\circ}21'36''$
<b>Associations</b>	
Kilonova association	Uncertain
SN association	Uncertain

**Table 2:** Individual burst properties of GRB 160425A.

	GRB 160425A- $G_1$		GRB 160425A- $G_2$	
	Value	Classification	Value	Classification
Time interval (15-350 keV) [ $t_1 \sim t_2$ ]	[-0.20~1.50] (s)		[257.0~308.2] (s)	
BAT-determined position [RA(J2000.0), Dec(J2000.0)]	[280.34°, -54.36°]		[280.29°, -54.35°]	
Duration (15-350 keV) [ $T_{90}$ ]	$1.7^{+0.5}_{-0.4}$ (s)	Short	$51.2^{+8.9}_{-9.2}$ (s)	Long
Hardness ratio [ $\frac{S(25-50\text{keV})}{S(15-25\text{keV})}$ ]	$1.74 \pm 0.09$	Short	$0.40 \pm 0.04$	Long
Minimum variability timescale (MVT)	$18.5 \pm 3.1$ (ms)	Short	$550 \pm 32$ (ms)	Long
$f(f_{\text{eff}})$ - parameter [ $F_p(F'_p)/F_b$ ]	$2.13 \pm 0.18$	Short	$1.05 \pm 0.03$	Long
Time lag [25-50 keV ~ 15-25 keV]	$(38 \pm 39)$ (ms)	Short	$(1152 \pm 264)$ (ms)	Long
Spectral photon index [ $\alpha$ ]	$-1.75 \pm 0.08$		$-1.17 \pm 0.02$	
Spectral peak energy [ $E_p$ ]	$\geq 500$ (keV)	Short	$57.6 \pm 2.7$ (keV)	Long
Bolometric (1-10 <sup>4</sup> keV) fluence [ $S_\gamma$ ]	$(8.6 \pm 1.1) \times 10^{-7}$ (erg cm <sup>-2</sup> )	Short	$(2.5 \pm 0.3) \times 10^{-6}$ (erg cm <sup>-2</sup> )	Long
Peak luminosity (15-150 keV) [ $L_{\gamma,p,\text{iso}}$ ]	$(2.0 \pm 0.2) \times 10^{50}$ (erg s <sup>-1</sup> )[64-ms]	Short	$(5.8 \pm 0.4) \times 10^{49}$ (erg s <sup>-1</sup> )[1-s]	Long
Isotropic energy (1-10 <sup>4</sup> keV) [ $E_{\gamma,\text{iso}}$ ]	$(7.2 \pm 0.9) \times 10^{50}$ (erg)	Short	$(2.1 \pm 0.3) \times 10^{51}$ (erg)	Long
$\varepsilon$ -parameter [ $E_{\gamma,\text{iso},52}/E_{p,z,2}^{5/3}$ ]	$0.002 \pm 0.001$	Short	$0.25 \pm 0.03$	Long
EHD-parameter [ $E_{p,i,2} E_{\text{iso},51}^{-0.4} T_{90,i}^{-0.5}$ ]	$9.5 \pm 2.1$	Short	$(1.2 \pm 0.1) \times 10^{-2}$	Long
Amati relation [ $E_{p,z} \propto E_{\gamma,\text{iso}}^{0.5}$ ]	Off the relation	Short	On the relation	Long
Norris relation [ $L_{\gamma,p,\text{iso}} \propto \tau^{-1.14}$ ]	Off the relation	Short	On the relation	Long

**Table 3:** A Phenomenological Classification of GRB Prompt Emission Light-Curve Morphologies and Their Physical Implications.

Phenomenological class	Representative events (e.g.)	Detected rate	Quiescent gap? (Background-consistent)	Traditional model (Obeyed/Violated)	Possible type	Reference (e.g.)
<b>Non-quiescent GRBs</b>						
(Single/overlapping emission episodes)						
Short-duration merger-like event	GRB 130603B	Commonly	No	Obeyed	Traditional Type I	(59)
Long-duration merger-like event	GRB 211211A	Rarely	No	Obeyed	Peculiar Type I	(32)
Continuous boundary/Hybrid event	GRB 180418A	Rarely	No	Obeyed	Type I or Type II	(60)
Short-duration collapsar-like event	GRB 200826A	Rarely	No	Obeyed	Peculiar Type II	(37)
Long-duration collapsar-like event	GRB 030329	Commonly	No	Obeyed	Traditional Type II	(61)
<b>Quiescent GRBs</b>						
(Two distinct emission episodes)						
Precursor( $G_1$ )+LGRB( $G_2$ )	GRB 160625B	Commonly	Yes	Obeyed	Traditional Type II	(47)
Double-main/trigger LGRB( $G_1+G_2$ )	GRB 110709B	Commonly	Yes	Obeyed	Traditional Type II	(62)
SGRB( $G_1$ )+extended emission( $G_2$ )	GRB 050709	Commonly	Yes	Obeyed	Traditional Type I	(18)
LGRB( $G_1$ )+late X-ray flare( $G_2$ )	GRB 050502B	Commonly	Yes	Obeyed	Traditional Type II	(41)
SGRB( $G_1$ )+late X-ray flare( $G_2$ )	GRB 050724	Commonly	Yes	Obeyed	Traditional Type I	(42)
LGRB( $G_1$ )+Afterglow onset( $G_2$ )	GRB 960530	Rarely	Yes	Obeyed	Traditional Type II	(43)
<b>SGRB(<math>G_1</math>)+LGRB(<math>G_2</math>)</b>	<b>GRB 160425A</b>	<b>The only one</b>	Yes	<b>Violated</b>	<b>Unclear</b>	<b>This paper</b>

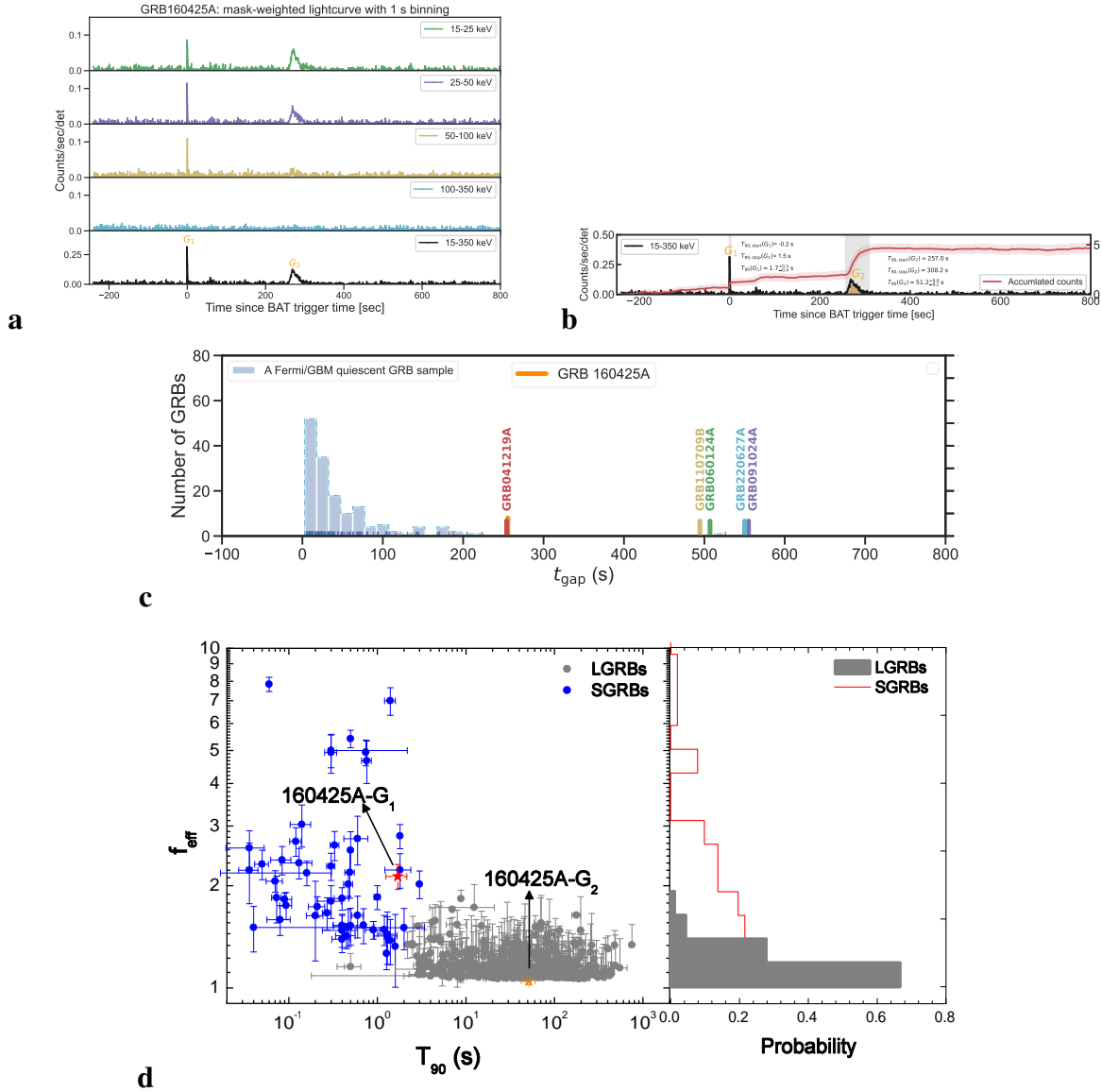


**Figure 1: Prompt  $\gamma$ -ray emission phase of GRB 160425A.** **a**, The background-subtracted light curves of GRB 160425A in distinct energy bands (15-25 keV: green, 25-50 keV: magenta, 50-100 keV: cyan, 100-350 keV: yellow, 15-350 keV: black), derived from *Swift*/BAT data. **b**,  $T_{90}$  analysis for the two individual bursts of GRB 160425A. The right panel displays the light curve across the full BAT energy range (15-350 keV), while the left panel shows the corresponding cumulative counts over time. **c**, GRB 160425A in the distribution of quiescent period  $t_{\text{gap}}$  in comparison with other significant quiescent gamma-ray bursts. **d**,  $T_{90}$ - $f(f_{\text{eff}})$  plot, where  $f$  represents the ratio between the peak flux and the average background flux of a GRB (Methods).  $f_{\text{eff}}$  is the effective  $f$  parameter, indicating how a long-duration GRB can be disguised as a short-duration GRB by arbitrarily lowering its flux level. The two distinct bursts of GRB 160425A are highlighted by the red ( $G_1$ ) and orange ( $G_2$ ) solid stars, respectively.

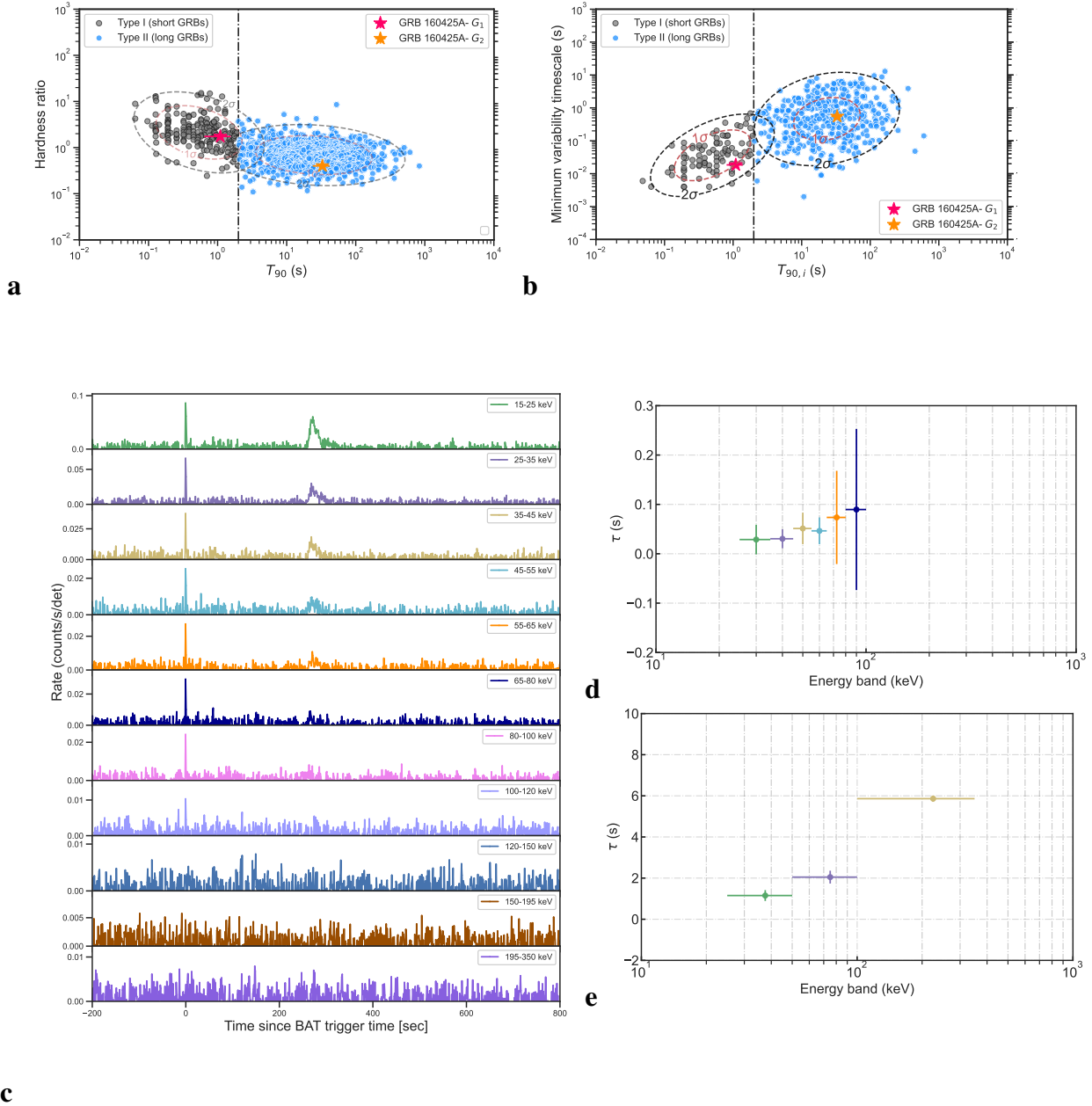


**Figure 2: GRB classification scheme.** **a-b**, The traditional GRB classification is illustrated based on the duration/hardness ratio diagram (**a**), and the duration/MVT diagram (**b**). The *Swift* GRB sample is represented by solid yellow and cyan points for the short-duration and long-duration burst populations, respectively. The two individual bursts of GRB 160425A are highlighted by red triangular and orange stars. Elliptical dotted lines in different colors indicate the  $1\sigma$  and  $2\sigma$  regions of the bivariate normal distributions for the short-duration and long-duration burst populations. The traditional separation line ( $t_{90} = 2$  s) between short-duration and long-duration GRBs is indicated by a black dashed vertical line. Duration is plotted in the observed frame for **a** and the source frame for **b**. **Spectral lag analysis (c-e).** **c**, Background-subtracted *Swift* light curves of GRB 160425A in different energy bands, used to calculate spectral lags. **d-e**, Energy-dependent spectral lag between the lowest energy band (15-25 keV) and higher energy band for the short-duration burst ( $G_1$ ) and the long-duration burst ( $G_2$ ) of GRB 160425A.

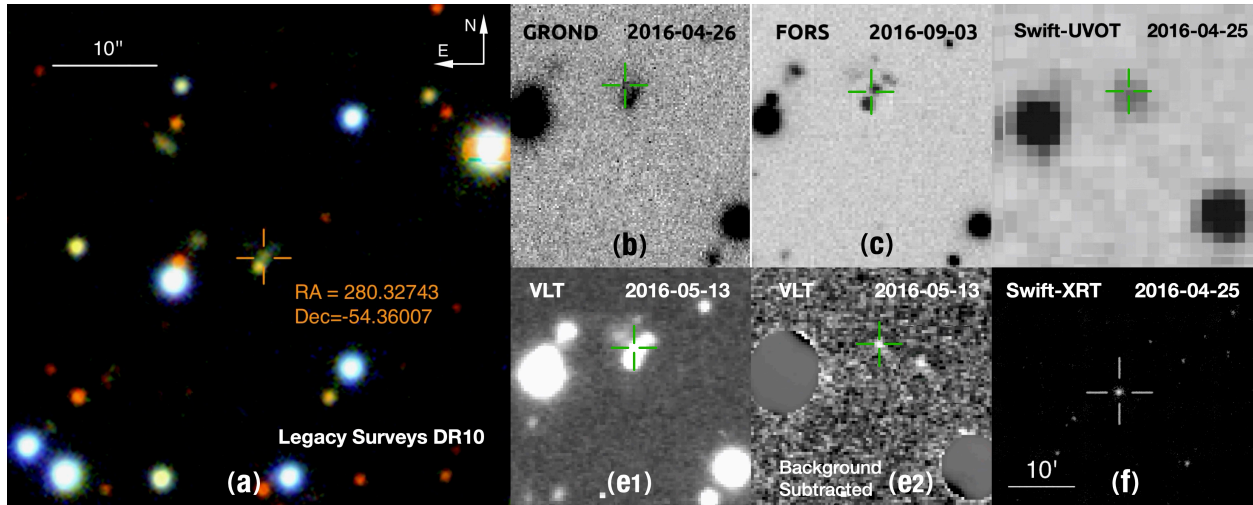


**Figure 3: Images of GRB 160425A and its host galaxy.** **Figure (a)** shows the survey data from DESI Legacy Surveys DR10, ref. (63), where the region with a knot structure at the center represents the host galaxy of GRB 160425A. **Figures (b) through (e)** present observations of the central celestial region in **Figure (a)**, captured by different optical telescopes at various times. Specifically, **Figure (b)** depicts observations by the GROND telescope on April 26, **Figure (c)** shows observations by the FORS telescope of the Very Large Telescope (VLT) on September 3, revealing three diffuse knots, and **Figure (d)** presents data from Swift-UVOT on April 25. **Figure (e1)** illustrates observations by the VLT on May 13, while **Figure (e2)** displays the same region as **Figure (e1)** with the background galaxies subtracted, revealing the optical image of the GRB. **Figure (f)** provides observations of soft X-rays by Swift-XRT on April 25, showcasing a larger field of view compared to the images mentioned above.

## References and Notes

1. C. Kouveliotou, *et al.*, Identification of two classes of gamma-ray bursts. *Astrophys. J. Lett.* **413**, L101–L104 (1993), doi:10.1086/186969.
2. S. E. Woosley, J. S. Bloom, The Supernova Gamma-Ray Burst Connection. *Annu. Rev. Astron. Astrophys.* **44**, 507–556 (2006), doi:10.1146/annurev.astro.43.072103.150558.
3. B. Zhang, Astrophysics: A burst of new ideas. *Nature* **444** (7122), 1010–1011 (2006), doi:10.1038/4441010a.
4. B. Zhang, *et al.*, Discerning the Physical Origins of Cosmological Gamma-ray Bursts Based on Multiple Observational Criteria: The Cases of  $z = 6.7$  GRB 080913,  $z = 8.2$  GRB 090423, and Some Short/Hard GRBs. *Astrophys. J.* **703** (2), 1696–1724 (2009), doi:10.1088/0004-637X/703/2/1696.
5. E. Berger, Short-Duration Gamma-Ray Bursts. *Annu. Rev. Astron. Astrophys.* **52**, 43–105 (2014), doi:10.1146/annurev-astro-081913-035926.
6. J. P. Norris, G. F. Marani, J. T. Bonnell, Connection between Energy-dependent Lags and Peak Luminosity in Gamma-Ray Bursts. *Astrophys. J.* **534** (1), 248–257 (2000), doi:10.1086/308725.
7. H.-J. Lü, E.-W. Liang, B.-B. Zhang, B. Zhang, A New Classification Method for Gamma-ray Bursts. *Astrophys. J.* **725** (2), 1965–1970 (2010), doi:10.1088/0004-637X/725/2/1965.
8. H.-J. Lü, B. Zhang, E.-W. Liang, B.-B. Zhang, T. Sakamoto, The ‘amplitude’ parameter of gamma-ray bursts and its implications for GRB classification. *Mon. Not. R. Astron. Soc.* **442** (3), 1922–1929 (2014), doi:10.1093/mnras/stu982.
9. Y.-P. Qin, Z.-F. Chen, Statistical classification of gamma-ray bursts based on the Amati relation. *Mon. Not. R. Astron. Soc.* **430** (1), 163–173 (2013), doi:10.1093/mnras/sts547.
10. Y. Li, B. Zhang, H.-J. Lü, A Comparative Study of Long and Short GRBs. I. Overlapping Properties. *Astrophys. J. Suppl.* **227** (1), 7 (2016), doi:10.3847/0067-0049/227/1/7.
11. P. Y. Minaev, A. S. Pozanenko, The  $E_{p,I}$ - $E_{iso}$  correlation: type I gamma-ray bursts and the new classification method. *Mon. Not. R. Astron. Soc.* **492** (2), 1919–1936 (2020), doi:10.1093/mnras/stz3611.
12. J. P. Norris, *et al.*, Long-Lag, Wide-Pulse Gamma-Ray Bursts. *Astrophys. J.* **627** (1), 324–345 (2005), doi:10.1086/430294.

13. I. Horváth, *et al.*, Detailed Classification of Swift 's Gamma-ray Bursts. *Astrophys. J.* **713** (1), 552–557 (2010), doi:10.1088/0004-637X/713/1/552.
14. A. Goldstein, *et al.*, An Ordinary Short Gamma-Ray Burst with Extraordinary Implications: Fermi-GBM Detection of GRB 170817A. *Astrophys. J. Lett.* **848** (2), L14 (2017), doi:10.3847/2041-8213/aa8f41.
15. V. Z. Golkhou, N. R. Butler, Uncovering the Intrinsic Variability of Gamma-Ray Bursts. *Astrophys. J.* **787** (1), 90 (2014), doi:10.1088/0004-637X/787/1/90.
16. V. Z. Golkhou, N. R. Butler, O. M. Littlejohns, The Energy Dependence of GRB Minimum Variability Timescales. *Astrophys. J.* **811** (2), 93 (2015), doi:10.1088/0004-637X/811/2/93.
17. J. P. Dezalay, *et al.*, Short Cosmic Events: A Subset of Classical GRBs?, in *American Institute of Physics Conference Series*, W. S. Paciesas, G. J. Fishman, Eds., vol. 265 of *American Institute of Physics Conference Series* (1992), p. 304.
18. J. P. Norris, J. T. Bonnell, Short Gamma-Ray Bursts with Extended Emission. *Astrophys. J.* **643** (1), 266–275 (2006), doi:10.1086/502796.
19. T. Yi, E. Liang, Y. Qin, R. Lu, On the spectral lags of the short gamma-ray bursts. *Mon. Not. R. Astron. Soc.* **367** (4), 1751–1756 (2006), doi:10.1111/j.1365-2966.2006.10083.x.
20. M. G. Bernardini, *et al.*, Comparing the spectral lag of short and long gamma-ray bursts and its relation with the luminosity. *Mon. Not. R. Astron. Soc.* **446** (2), 1129–1138 (2015), doi:10.1093/mnras/stu2153.
21. L. Amati, *et al.*, Intrinsic spectra and energetics of BeppoSAX Gamma-Ray Bursts with known redshifts. *Astro., Astrophys.* **390**, 81–89 (2002), doi:10.1051/0004-6361:20020722.
22. H. A. Krimm, *et al.*, GRB 160425A: Swift detection of an unusual burst with an optical afterglow. *GRB Coordinates Network* **19343**, 1 (2016).
23. A. Melandri, *et al.*, GRB 160425A: Swift-XRT refined Analysis. *GRB Coordinates Network* **19348**, 1 (2016).
24. J. Bodensteiner, S. Schmidl, J. Greiner, GRB 160425A: GROND observation. *GRB Coordinates Network* **19349**, 1 (2016).
25. B. E. Cobb, GRB 160425A: SMARTS optical/IR observations. *GRB Coordinates Network* **19354**, 1 (2016).
26. M. H. Siegel, H. A. Krimm, GRB 160425A: Swift/UVOT Detection. *GRB Coordinates Network* **19357**, 1 (2016).

27. N. R. Tanvir, *et al.*, GRB 160425A VLT/X-shooter redshift. *GRB Coordinates Network* **19350**, 1 (2016).
28. Z. Zhang, G. Z. Xie, J. G. Deng, W. Jin, Revisiting the characteristics of the spectral lags in short gamma-ray bursts. *Mon. Not. R. Astron. Soc.* **373** (2), 729–732 (2006), doi:10.1111/j.1365-2966.2006.11058.x.
29. J. P. U. Fynbo, *et al.*, No supernovae associated with two long-duration  $\gamma$ -ray bursts. *Nature* **444** (7122), 1047–1049 (2006), doi:10.1038/nature05375.
30. A. Gal-Yam, *et al.*, A novel explosive process is required for the  $\gamma$ -ray burst GRB 060614. *Nature* **444** (7122), 1053–1055 (2006), doi:10.1038/nature05373.
31. N. Gehrels, *et al.*, A new  $\gamma$ -ray burst classification scheme from GRB060614. *Nature* **444** (7122), 1044–1046 (2006), doi:10.1038/nature05376.
32. J. C. Rastinejad, *et al.*, A kilonova following a long-duration gamma-ray burst at 350 Mpc. *Nature* **612** (7939), 223–227 (2022), doi:10.1038/s41586-022-05390-w.
33. E. Troja, *et al.*, A nearby long gamma-ray burst from a merger of compact objects. *Nature* **612** (7939), 228–231 (2022), doi:10.1038/s41586-022-05327-3.
34. J. Yang, *et al.*, A long-duration gamma-ray burst with a peculiar origin. *Nature* **612** (7939), 232–235 (2022), doi:10.1038/s41586-022-05403-8.
35. A. J. Levan, *et al.*, Heavy-element production in a compact object merger observed by JWST. *Nature* **626** (8000), 737–741 (2024), doi:10.1038/s41586-023-06759-1.
36. Y.-H. Yang, *et al.*, A lanthanide-rich kilonova in the aftermath of a long gamma-ray burst. *Nature* **626** (8000), 742–745 (2024), doi:10.1038/s41586-023-06979-5.
37. B.-B. Zhang, *et al.*, A peculiarly short-duration gamma-ray burst from massive star core collapse. *Nature Astronomy* **5**, 911–916 (2021), doi:10.1038/s41550-021-01395-z.
38. L. Li, Y. Wang, J.-J. Geng, Y.-F. Huang, R.-G. Cai, Pulse-resolved Classification and Characteristics of Long-duration Gamma-Ray Bursts with Swift-BAT Data. I. Precursors versus Main Bursts. *Astrophys. J. Suppl.* **283** (2), 47 (2026), doi:10.3847/1538-4365/ae47e7.
39. L. Li, *et al.*, Pulse-resolved Classification and Characteristics of Long-duration GRBs with Swift-BAT Data.II. Main Burst versus Extended Emission. *arXiv e-prints* arXiv:2602.22926 (2026), doi:10.48550/arXiv.2602.22926.
40. L. Li, Classification and Characteristics of Double-trigger Gamma-ray Bursts. *arXiv e-prints* arXiv:2512.23660 (2025), doi:10.48550/arXiv.2512.23660.

41. A. D. Falcone, *et al.*, The Giant X-Ray Flare of GRB 050502B: Evidence for Late-Time Internal Engine Activity. *Astrophys. J.* **641** (2), 1010–1017 (2006), doi:10.1086/500655.
42. Z. G. Dai, X. Y. Wang, X. F. Wu, B. Zhang, X-ray Flares from Postmerger Millisecond Pulsars. *Science* **311**, 1127–1129 (2006), doi:10.1126/science.1123606.
43. J. Hakkila, T. W. Giblin, Quiescent Burst Evidence for Two Distinct Gamma-Ray Burst Emission Components. *Astrophys. J.* **610** (1), 361–367 (2004), doi:10.1086/421060.
44. L. Li, *et al.*, A Correlated Study of Optical and X-Ray Afterglows of GRBs. *Astrophys. J.* **805** (1), 13 (2015), doi:10.1088/0004-637X/805/1/13.
45. L. Li, *et al.*, Constraining the Type of Central Engine of GRBs with Swift Data. *Astrophys. J. Suppl.* **236** (2), 26 (2018), doi:10.3847/1538-4365/aabaf3.
46. R. Ruffini, *et al.*, Early X-Ray Flares in GRBs. *Astrophys. J.* **852**, 53 (2018), doi:10.3847/1538-4357/aa9e8b.
47. B. Zhang, *The Physics of Gamma-Ray Bursts* (2018), doi:10.1017/9781139226530.
48. B. E. Cobb, GRB 160425A: SMARTS late-time observations. *GRB Coordinates Network* **19454**, 1 (2016).
49. R. Margutti, *et al.*, X-ray flare candidates in short gamma-ray bursts. *Mon. Not. R. Astron. Soc.* **417** (3), 2144–2160 (2011), doi:10.1111/j.1365-2966.2011.19397.x.
50. B.-B. Zhang, *et al.*, Transition from fireball to Poynting-flux-dominated outflow in the three-episode GRB 160625B. *Nature Astronomy* **2**, 69–75 (2018), doi:10.1038/s41550-017-0309-8.
51. F. Ryde, *et al.*, Onset of Particle Acceleration during the Prompt Phase in Gamma-Ray Bursts as Revealed by Synchrotron Emission in GRB 160821A. *Astrophys. J. Lett.* **932** (2), L15 (2022), doi:10.3847/2041-8213/ac73fe.
52. D. Burlon, *et al.*, Precursors in Swift Gamma Ray Bursts with Redshift. *Astrophys. J. Lett.* **685** (1), L19 (2008), doi:10.1086/592350.
53. D. Burlon, G. Ghirlanda, G. Ghisellini, J. Greiner, A. Celotti, Time resolved spectral behavior of bright BATSE precursors. *Astro., Astrophys.* **505** (2), 569–575 (2009), doi:10.1051/0004-6361/200912662.
54. Y.-D. Hu, *et al.*, Internal Energy Dissipation of Gamma-Ray Bursts Observed with Swift: Precursors, Prompt Gamma-Rays, Extended Emission, and Late X-Ray Flares. *Astrophys. J.* **789**, 145 (2014), doi:10.1088/0004-637X/789/2/145.

55. N. Anand, M. Shahid, L. Resmi, Merger delay time distribution of extended emission short GRBs. *Mon. Not. R. Astron. Soc.* **481** (4), 4332–4341 (2018), doi:10.1093/mnras/sty2530.
56. X. J. Li, Z. B. Zhang, X. L. Zhang, H. Y. Zhen, Temporal Properties of Precursors, Main Peaks, and Extended Emissions of Short GRBs in the Third Swift/BAT GRB Catalog. *Astrophys. J. Suppl.* **252** (2), 16 (2021), doi:10.3847/1538-4365/abd3fd.
57. H.-Y. Deng, Z.-Y. Peng, J.-M. Chen, Y. Yin, T. Li, A Study of the Spectral Properties of Gamma-Ray Bursts with the Precursors and Main Bursts. *Astrophys. J.* **970** (1), 67 (2024), doi:10.3847/1538-4357/ad4d95.
58. J.-J. Geng, B. Zhang, R. Kuiper, Propagation of Relativistic, Hydrodynamic, Intermittent Jets in a Rotating, Collapsing GRB Progenitor Star. *Astrophys. J.* **833** (1), 116 (2016), doi:10.3847/1538-4357/833/1/116.
59. N. R. Tanvir, *et al.*, A ‘kilonova’ associated with the short-duration  $\gamma$ -ray burst GRB 130603B. *Nature* **500** (7464), 547–549 (2013), doi:10.1038/nature12505.
60. R. L. Becerra, *et al.*, Reverse Shock Emission Revealed in Early Photometry in the Candidate Short GRB 180418A. *Astrophys. J.* **881** (1), 12 (2019), doi:10.3847/1538-4357/ab275b.
61. J. Hjorth, *et al.*, A very energetic supernova associated with the  $\gamma$ -ray burst of 29 March 2003. *Nature* **423** (6942), 847–850 (2003), doi:10.1038/nature01750.
62. B.-B. Zhang, *et al.*, Unusual Central Engine Activity in the Double Burst GRB 110709B. *Astrophys. J.* **748** (2), 132 (2012), doi:10.1088/0004-637X/748/2/132.
63. A. Dey, *et al.*, Overview of the DESI Legacy Imaging Surveys. *Astronom. J.* **157** (5), 168 (2019), doi:10.3847/1538-3881/ab089d.
64. L. Lan, *et al.*, Characteristics of Two-episode Emission Patterns in Fermi Long Gamma-Ray Bursts. *Astrophys. J.* **862** (2), 155 (2018), doi:10.3847/1538-4357/aacda6.
65. L. Li, J. Mao, Temporal Analysis of GRB Precursors in the Third Swift-BAT Catalog. *Astrophys. J.* **928** (2), 152 (2022), doi:10.3847/1538-4357/ac4af2.
66. P. A. Evans, *et al.*, An online repository of Swift/XRT light curves of  $\gamma$ -ray bursts. *Astro., Astrophys.* **469**, 379–385 (2007), doi:10.1051/0004-6361:20077530.
67. P. A. Evans, *et al.*, Methods and results of an automatic analysis of a complete sample of Swift-XRT observations of GRBs. *Mon. Not. R. Astron. Soc.* **397**, 1177–1201 (2009), doi:10.1111/j.1365-2966.2009.14913.x.

68. G. Vianello, *et al.*, The Multi-Mission Maximum Likelihood framework (3ML). *arXiv e-prints* (2015).
69. P. Romano, *et al.*, Panchromatic study of GRB 060124: from precursor to afterglow. *Astro., Astrophys.* **456** (3), 917–927 (2006), doi:10.1051/0004-6361:20065071.
70. W. Cash, Parameter estimation in astronomy through application of the likelihood ratio. *ApJ* **228**, 939–947 (1979), doi:10.1086/156922.
71. J. S. Bloom, D. A. Frail, R. Sari, The Prompt Energy Release of Gamma-Ray Bursts using a Cosmological k-Correction. *aj* **121**, 2879–2888 (2001), doi:10.1086/321093.
72. P. A. Evans, *et al.*, 1SXPS: A Deep Swift X-Ray Telescope Point Source Catalog with Light Curves and Spectra. *Astrophys. J. Suppl.* **210** (1), 8 (2014), doi:10.1088/0067-0049/210/1/8.
73. L. X. Cheng, Y. Q. Ma, K. S. Cheng, T. Lu, Y. Y. Zhou, The time delay of gamma-ray bursts in the soft energy band. *Astro., Astrophys.* **300**, 746 (1995).
74. D. L. Band, Gamma-Ray Burst Spectral Evolution through Cross-Correlations of Discriminator Light Curves. *Astrophys. J.* **486**, 928–937 (1997), doi:10.1086/304566.
75. T. N. Ukwatta, *et al.*, Spectral Lags and the Lag-Luminosity Relation: An Investigation with Swift BAT Gamma-ray Bursts. *Astrophys. J.* **711**, 1073–1086 (2010), doi:10.1088/0004-637X/711/2/1073.
76. L. Li, Y. Wang, A Novel Method of Estimating Gamma-Ray Burst Peak Energies beyond the Swift/BAT Limit. *Astrophys. J. Suppl.* **283** (1), 18 (2026), doi:10.3847/1538-4365/ae36a5.
77. Planck Collaboration, *et al.*, Planck 2018 results. VI. Cosmological parameters. *arXiv e-prints* arXiv:1807.06209 (2018).
78. M. Newville, *et al.*, LMFIT: Non-linear least-square minimization and curve-fitting for Python. *ascl* pp. ascl–1606 (2016).
79. P. W. A. Roming, *et al.*, The Swift Ultra-Violet/Optical Telescope. *Spa., Sci., Rev.* **120** (3-4), 95–142 (2005), doi:10.1007/s11214-005-5095-4.
80. E. F. Schlafly, D. P. Finkbeiner, Measuring Reddening with Sloan Digital Sky Survey Stellar Spectra and Recalibrating SFD. *ApJ* **737**, 103 (2011), doi:10.1088/0004-637X/737/2/103.
81. J. B. Oke, A. Sandage, Energy Distributions, K Corrections, and the Stebbins-Whitford Effect for Giant Elliptical Galaxies. *Astrophys. J.* **154**, 21 (1968), doi:10.1086/149737.

82. B. M. Peterson, *An Introduction to Active Galactic Nuclei* (Cambridge University Press) (1997).
83. L. Li, *et al.*, A Large Catalog of Multiwavelength GRB Afterglows. I. Color Evolution and Its Physical Implication. *Astrophys. J. Suppl.* **234** (2), 26 (2018), doi:10.3847/1538-4365/aaa02a.
84. Pei, Y C, Interstellar dust from the Milky Way to the Magellanic Clouds. *ApJ* (1992).
85. Z. Cano, S.-Q. Wang, Z.-G. Dai, X.-F. Wu, The Observer's Guide to the Gamma-Ray Burst Supernova Connection. *Advances in Astronomy* **2017**, 8929054 (2017), doi:10.1155/2017/8929054.
86. N. R. Tanvir, *et al.*, GRB 160425A VLT/X-shooter redshift. *GRB Coordinates Network* **19350**, 1 (2016).
87. D. Calzetti, Reddening and Star Formation in Starburst Galaxies. *Astronom. J.* **113**, 162–184 (1997), doi:10.1086/118242.
88. A. Clocchiatti, N. B. Suntzeff, R. Covarrubias, P. Candia, The Ultimate Light Curve of SN 1998bw/GRB 980425. *Astronom. J.* **141**, 163 (2011), doi:10.1088/0004-6256/141/5/163.
89. A. Zeh, S. Klose, D. H. Hartmann, A Systematic Analysis of Supernova Light in Gamma-Ray Burst Afterglows. *Astrophys. J.* **609** (2), 952–961 (2004), doi:10.1086/421100.
90. G. Ryan, H. van Eerten, L. Piro, E. Troja, Gamma-Ray Burst Afterglows in the Multimessenger Era: Numerical Models and Closure Relations. *Astrophys. J.* **896** (2), 166 (2020), doi:10.3847/1538-4357/ab93cf.
91. J. Selsing, *et al.*, The X-shooter GRB afterglow legacy sample (XS-GRB). *Astro., Astrophys.* **623**, A92 (2019), doi:10.1051/0004-6361/201832835.
92. A. Stroe, V.-N. Savu, GLEAM: Galaxy Line Emission & Absorption Modeling. *Astronom. J.* **161** (4), 158 (2021), doi:10.3847/1538-3881/abe12a.
93. E. F. Schlafly, D. P. Finkbeiner, Measuring Reddening with Sloan Digital Sky Survey Stellar Spectra and Recalibrating SFD. *Astrophys. J.* **737** (2), 103 (2011), doi:10.1088/0004-637X/737/2/103.
94. R. C. Kennicutt, N. J. Evans, Star Formation in the Milky Way and Nearby Galaxies. *Annu. Rev. Astron. Astrophys.* **50**, 531–608 (2012), doi:10.1146/annurev-astro-081811-125610.
95. M. Pettini, B. E. J. Pagel, [OIII]/[NII] as an abundance indicator at high redshift. *Mon. Not. R. Astron. Soc.* **348** (3), L59–L63 (2004), doi:10.1111/j.1365-2966.2004.07591.x.

96. W. Freudling, *et al.*, Automated data reduction workflows for astronomy. The ESO Reflex environment. *Astro., Astrophys.* **559**, A96 (2013), doi:10.1051/0004-6361/201322494.
97. E. Bertin, S. Arnouts, SExtractor: Software for source extraction. *Astro., Astrophys., Suppl* **117**, 393–404 (1996), doi:10.1051/aas:1996164.
98. E. Bertin, Automatic Astrometric and Photometric Calibration with SCAMP, in *Astronomical Data Analysis Software and Systems XV*, C. Gabriel, C. Arviset, D. Ponz, S. Enrique, Eds., vol. 351 of *Astronomical Society of the Pacific Conference Series* (2006), p. 112.
99. E. Bertin, *et al.*, The TERAPIX Pipeline, in *Astronomical Data Analysis Software and Systems XI*, D. A. Bohlender, D. Durand, T. H. Handley, Eds., vol. 281 of *Astronomical Society of the Pacific Conference Series* (2002), p. 228.
100. W.-f. Fong, *et al.*, Short GRB Host Galaxies. I. Photometric and Spectroscopic Catalogs, Host Associations, and Galactocentric Offsets. *Astrophys. J.* **940** (1), 56 (2022), doi:10.3847/1538-4357/ac91d0.
101. F. J. Virgili, *et al.*, GRB 091024A and the Nature of Ultra-long Gamma-Ray Bursts. *Astrophys. J.* **778**, 54 (2013), doi:10.1088/0004-637X/778/1/54.
102. Y.-Y. Huang, H.-M. Zhang, K. Yan, R.-Y. Liu, X.-Y. Wang, Detection of GeV Emission from an Ultralong Gamma-Ray Burst with the Fermi Large Area Telescope. *Astrophys. J. Lett.* **940** (2), L36 (2022), doi:10.3847/2041-8213/aca147.
103. L. Li, Multipulse Fermi Gamma-Ray Bursts. I. Evidence of the Transition from Fireball to Poynting-flux-dominated Outflow. *Astrophys. J. Suppl.* **242** (2), 16 (2019), doi:10.3847/1538-4365/ab1b78.
104. S. de Wet, *et al.*, The ultra-long GRB 220627A at  $z = 3.08$ . *Astro., Astrophys.* **677**, A32 (2023), doi:10.1051/0004-6361/202347017.
105. Y.-R. Shi, X.-K. Ding, S.-Y. Zhu, W.-P. Sun, F.-W. Zhang, Statistical Properties of X-ray Flares in Gamma-Ray Bursts. *Universe* **8** (7), 358 (2022), doi:10.3390/universe8070358.
106. G. Chincarini, *et al.*, Unveiling the origin of X-ray flares in gamma-ray bursts. *Mon. Not. R. Astron. Soc.* **406** (4), 2113–2148 (2010), doi:10.1111/j.1365-2966.2010.17037.x.

## Acknowledgments

We acknowledge the use of public data from the Fermi Science Support Center, Swift Science Data Centre, and GCN circulars reported by multiple facilities. LL thanks Filip Alamaa, Nathaniel R. Butler, Kim Page, Luca Izzo, Pat Schady, Tyler Parsotan, Xue-Feng Wu, Wei-Min Gu, Wei-Min Yuan, Di Li, Jun-Hui Fan, En-Wei Liang, Amy Lien, Soroush Shakeri, and the ICRANet members for many helpful discussions on data analysis, GRB physics and phenomena.

**Funding:** The authors were supported by the National Natural Science Foundation of China (NSFC), grant numbers 12233002 (YFH), 11874033 (LL), and 12588101 (LL and RGC). LL also acknowledges support from the KC Wong Magna Foundation at Ningbo University. The computations were supported by the high-performance computing center at Ningbo University.

**Author contributions:** LL and YW initiated the study and coordinated the scientific investigations of the event. BZ and RGC were in charge of the framework of this article. LL organized the paper, led the data analysis, and contributed to part of the physical explanations. YW discovered this particular event, assisted in the data analysis, and contributed to the theoretical explanation. LL and YW processed and analyzed the *Swift*/BAT, *Swift*/XRT data, and multi-wavelength afterglow observations. LL calculated the hardness ratio, the amplitude parameter, the spectral analysis, the Amati correlation, the spectral lags, the minimum variability timescale, the Norris correlation, the EHD parameter, and the  $\epsilon$  parameter. BZ, SNZ, SRZ, YFY, JJG and RGC proposed the model to explain the observed data. JG processed and analyzed the GROND data and contributed information about the host galaxy. YL, ZPJ, and YZF processed and analyzed the VLT data and contributed information about the host galaxy. LL, YW, LY, and BZ wrote the manuscript with contributions from all authors. All authors have reviewed, discussed, and commented on the present results and the manuscript.

## Author information:

Correspondence and requests for materials should be addressed to LL (liliang@nbu.edu.cn), YW (yu.wang@inaf.it), BZ (zhang@physics.unlv.edu), and RGC (cairg@itp.ac.cn).

**Competing interests:** The authors declare no competing interests.

**Data and materials availability:** The processed data are presented in the tables and figures of the paper. The code (all in Python) used to produce the results and figures will be provided. The

authors point out that some data used in the paper are publicly available, either through the UK Swift Science Data Centre website, JWST website, or GCN circulars.

## **Supplementary materials**

Materials and Methods

Supplementary Text

Figs. S1 to S7

Tables S1 to S6

References (59-106)

# Supplementary Materials for An Intertwined Short and Long GRB with 4-minute Separation

Liang Li<sup>1,2\*</sup>, Yu Wang<sup>3,4,5†</sup>, Bing Zhang<sup>6,7,8\*</sup>, Ye Li<sup>9</sup>, Shu-Rui Zhang<sup>10</sup>, Jochen Greiner<sup>11</sup>,  
Zhi-Ping Jin<sup>7</sup>, Jin-Jun Geng<sup>7</sup>, Hou-Jun Lü<sup>12</sup>, Asaf Pe'er<sup>13</sup>, Maria Dainotti<sup>14</sup>, Tong Liu<sup>15</sup>,  
Yi-Zhong Fan<sup>7</sup>, Yong-Feng Huang<sup>16,17</sup>, Zi-Gao Dai<sup>10</sup>, Melin Kole<sup>16,17</sup>, Wei-Hua Lei<sup>20</sup>,  
Ye-Fei Yuan<sup>10</sup>, Shuang-Nan Zhang<sup>21</sup>, Felix Ryde<sup>22</sup>, She-Sheng Xue<sup>3,4</sup>, Rong-Gen Cai<sup>1\*</sup>

\*Corresponding author. Email: liliang@nbu.edu.cn (L.L.); yu.wang@inaf.it (Y.W.);  
zhang@physics.unlv.edu (B.Z.); cairg@itp.ac.cn (R.G.C.)

## Materials and Methods

### Uniqueness of GRB 160425A in the Overall GRB Population.

GRB 160425A is unique in terms of the following three aspects. (1) It features two distinct emission episodes, an initial sub-burst, designated  $G_1$ , followed by a second,  $G_2$ . The two sub-bursts exhibit a quiescent interval measuring approximately 256 seconds in the observed frame and about 165 seconds in the rest frame, making GRB 160425A one of the longest quiescent gaps observed between GRB pulses. (2) The initial sub-burst,  $G_1$ , displays a sharp, single-peaked light curve and a short duration ( $\sim 1.7$  s), appearing like a traditional short-duration GRB. Conversely, the subsequent sub-burst,  $G_2$ , exhibits a broad, single-peaked light curve and long duration ( $\sim 51.2$  s), aligning with the characteristic of a traditional long-duration GRB. (3) During its prompt emission phase, nearly all standard diagnostics for GRB classifications consistently categorize  $G_1$  as a short-like (Type-I merger-origin) event and  $G_2$  as a long-like (Type-II collapsar-origin) event. These diagnostics include key parameters such as duration, pulse shape, minimum variability, spectral lag, hardness ratio, EHD and  $\epsilon$  parameters, along with the Amati and Norris correlations. These compelling and consistent findings rule out alternative interpretations, such as the occasional occurrence of precursors or flares often observed during burst processes. These properties together make GRB 160425A a unique event, providing a solid identification for a transition from short-like (Type-I merger-origin) event to long-like (Type-II collapsar-origin) event within a single system.

### Quiescent gap ( $t_{\text{gap}}$ ) of GRB 160425A.

To assess whether the quiescent gap observed in GRB 160425A is unique, we compiled a comprehensive dataset of “quiescent” GRBs by combining data from two independent studies (64, 65). These studies systematically analyzed quiescent times from “quiescent” GRB samples detected by *Swift* and *Fermi*. Our compiled dataset comprises 102 Fermi-detected GRBs (64) and 52 *Swift*-detected GRBs (65). Figure 1b presents the distribution of quiescent times ( $\Delta t_{\text{gap}}$ ) within this dataset and GRB 160425A and other significant quiescent events highlighted within the distribution.

Remarkably, among all the bursts in the sample, only a handful of events exhibit a quiescent gap longer than or comparable to that of GRB 160425A. These events include GRB 041219A and GRB 060124A, as well as three double-tracking GRBs: GRB 091024A, GRB 110709B, and GRB 220627A.

### *Swift* Data Retrieved.

We retrieve the *Swift* data from the UK *Swift* Science Data Centre (UKSSDC, <https://www.swift.ac.uk>). Data reduction was performed using HEASoft 6.30 and relevant calibration files (<http://heasarc.gsfc.nasa.gov/lheasoft/>). The Fermi Online Server ([S2](https://apps.</a></p></div><div data-bbox=)

sciserver.org/dashboard/) at the Fermi Science Support Center (FSSC, <https://fermi.gsfc.nasa.gov/ssc/>) was utilized for data processing. We conducted the extraction of photon events and subsequent temporal and spectral analysis following the methodologies outlined in (66, 67). Moreover, our analysis is double-checked by implementing the Multi-Mission Maximum Likelihood framework (3ML) (68) via the exported spectra nested in the 3ML package as a plugin.

### **Prompt Emission Light Curve Analysis.**

Using the *Swift*-BAT data obtained from the *Swift* archive website (<https://www.swift.ac.uk/archive/q1.php>), we generated the *Swift*-BAT light curve. HEASoft tools (version 6.30) were employed following standard analysis threads (<https://www.swift.ac.uk/analysis/bat/>). We use *batbinevt* to create the 1024-ms light curves employing a uniform-bin method across four standard *Swift*-BAT energy bands: 15-25 keV, 25-50 keV, 50-100 keV, and 100-350 keV. The light curves for different energy bands are illustrated in Figure 1, revealing a singular sharp-peaked structure ( $G_1$ ) lasting approximately 1.7 seconds, succeeded by a broader peak ( $G_2$ ) lasting  $\sim 51.2$  seconds at  $T_0+257.0$  s, separated by a long quiescent period ( $\sim 250$  s). By computing the cumulative photon distribution across the entire BAT energy band (15-350 keV), we obtained the  $T_{90}$  for both short-duration and long-duration bursts (see Figure 1), representing the duration between the epochs encompassing 5% and 95% of the total fluence. The  $1\sigma$  error region of the cumulative photon distribution was also determined by cumulatively summing the error of photon rate (counts/s/det) for each time bin (indicated in pink in Figure 1). From the sharp peak occurring between  $T_0-0.2$  and  $T_0+1.5$  s of the short burst  $G_1$ , we computed  $T_{90} \sim 1.7$  s. Similarly, for the broad peak  $G_2$  spanning  $T_0+257.0$  to  $T_0+308.2$  s, we determined  $T_{90} \sim 51.2$  s.

### ***Swift*-BAT Spectral Data Analysis.**

With the BAT data downloaded from *Swift* archive website, we then use *batbinevt*, *batupdatephakw*, *batphasyserr*, and *batdrngen* to generate the spectral and relevant response files, including accumulated BAT event and DPH data into spectra (*batbinevt*), updating BAT ray tracing columns in spectral files (*batupdatephakw*), applying the BAT spectral systematic error vector (*batphasyserr*), and computing a BAT detector response matrix (RSP) for a known source position (*batdrngen*). Using the generated spectral and response files, we conducted time-integrated spectral analysis within the  $T_{90}$  time intervals determined by the cumulative photon distribution for both  $G_1$  and  $G_2$ . We used the typical spectral fitting models, such as the simple power-law (PL), cutoff power-law (CPL), Band function (Band), and blackbody (BB), along with their hybrid versions to fit the spectra. Initially, spectral fitting was performed using XSPEC, followed by double-checking the fit results by implementing the 3ML via the exported spectra nested in the 3ML package as a plugin. For  $G_1$  ( $T_0-0.20$  to  $T_0+1.50$  s), the spectral fitting did not reveal a distinct peak within the BAT

energy range, suggesting that BB, CPL, or Band models may not adequately describe the data. Consequentially, the peak energy  $E_p$  must lie beyond the BAT energy range (15-150 keV) to avoid divergence of luminosity beyond this range. For  $G_2$  ( $T_0+257.0$  to  $T_0+308.02$  s), a spectral peak was observed in the fitting, with the Band model presenting the best fit. The resulting parameters included a low-energy photon index  $\alpha = -1.17 \pm 0.10$ , a high photon index  $\beta = -2.44 \pm 0.08$ , and the peak energy  $E_p = 57.6 \pm 2.7$  keV. The photon number spectra of the PL & Band models can be described as

$$N(E) = A \left( \frac{E}{E_{\text{piv}}} \right)^{\Gamma_{\text{PL}}}, \quad (\text{S1})$$

and

$$N(E) = A \begin{cases} \left( \frac{E}{E_{\text{piv}}} \right)^{\alpha} \exp\left(-\frac{E}{E_0}\right), & E \leq (\alpha - \beta)E_0 \\ \left[ \frac{(\alpha - \beta)E_0}{E_{\text{piv}}} \right]^{(\alpha - \beta)} \exp(\beta - \alpha) \left( \frac{E}{E_{\text{piv}}} \right)^{\beta}, & E \geq (\alpha - \beta)E_0 \end{cases} \quad (\text{S2})$$

respectively, where  $A$  is the normalization factor at 100 keV in units of  $\text{ph cm}^{-2}\text{keV}^{-1}\text{s}^{-1}$ ,  $E_{\text{piv}}$  is the pivot energy fixed at 100 keV,  $\Gamma_{\text{PL}}$  is the power-law photon index, and  $\alpha$  and  $\beta$  are the low- and high-energy power-law photon spectral indices, respectively.  $E_p$  represents the peak energy, which is related to  $E_0$  through the equation  $E_p = (2 + \alpha)E_0$ .

### **Swift-XRT Spectral Data Analysis.**

The *Swift*-XRT data were acquired from the *Swift* archive website, focusing on the time-sliced spectrum between  $T_0+257.0$  and  $T_0+308.2$  s, corresponding to the duration of  $G_2$ . This time interval was chosen to ensure consistency with the temporal characteristics of the long-duration burst, as no X-ray counterparts were observed during the epoch of  $G_1$ . The *Swift*-XRT instrument provides high-resolution X-ray data of GRB afterglows. We first retrieve its raw data from UKSSDC, followed by the data reduction procedure using the HEASoft 6.30 and relevant calibration files. The position of the source is determined by fitting the X-ray point spread function, or taken from the UVOT observation if it exists, approximately 75% positions are enhanced by the UVOT observation ([http://www.swift.ac.uk/xrt\\_positions/](http://www.swift.ac.uk/xrt_positions/)). XSELECT is adopted to extract images, light curves, and spectra (66, 67), and the related pile-up effect is corrected if necessary. We follow the suggestion by *Swift* data reduction guide (<http://www.swift.ac.uk/analysis/>), that the threshold of applying pile-up correction is given as, for windows timing data, the count rate is above 100 counts/s; and for photon counting data, the count rate exceeds 0.5 counts/s, the detailed method follows (69). XSPEC is adopted for fitting the spectrum, which is binned as at least 1 count per bin by GRPPHA to ensure the validity of Cash-statistics (70). Generally, a single power-law model combined with the hydrogen absorption from the host galaxy and our Galaxy is preferred, but for rigorous, we also check the existence of an extra thermal component, the method of the maximum likelihood ratio is employed to select one from two nested models by comparing the

statistical significance. The uncertainty of the fitted parameters is estimated for a 90% confidence level by the ERROR command and examined by the Monte Carlo Markov Chain iteration using the CHAIN command.

Our refined spectral analysis revealed that the *Swift*-XRT data during the X-ray flare phase (between 257.0 and 308.2 seconds, corresponding to the epoch of  $G_2$ ) could be accurately described by a simple power-law model, yielding a power-law index of  $\Gamma = 1.75 \pm 0.05$ . Subsequently, the X-ray light curve was transformed into its corresponding cosmological rest frame, with appropriate  $k$ -correction applied (71). Further details regarding the XRT automated analysis methods can be found in Refs (66, 67, 72).

### **Fermi-GBM Signal Search and Data Analysis (Untriggered).**

We obtained the position history (POSHIST) data of the Fermi satellite from the Fermi GBM Daily Data<sup>2</sup> for April 25, 2016. At the time when *Swift*-BAT was triggered, 23:26:11 UT, the Fermi satellite and GRB 160425A were located on opposite sides of the Earth. In other words, the GRB was blocked by the Earth, and the Fermi satellite was unable to observe it, see Figure S7a, the red pentagram represents GRB 160425A, and the blue region represents the Earth. We also plotted the light curve of all-sky observed by Fermi, see Figure S7b, there is no clear signal 5 minutes before and after the trigger time.

### **Hardness Ratio.**

It has been observed that short-duration GRBs tend to exhibit harder spectra compared to typical long-duration GRBs (17). To quantify this, we define a hardness ratio as the observed photon counts ratio between the 25-50 keV and 15-25 keV energy bands. For  $G_1$ , we compare the observed counts between  $T_0-0.20$  and  $T_0+1.50$  s, while for  $G_2$ , the comparison is made between  $T_0+257.0$  and  $T_0+308.2$  s. The individual bursts of GRB 160425A are indicated by a colored star in Figure 2a, while the *Swift* GRB sample (13), categorized into short-duration, and long-duration GRB populations (1), is represented by colored points. As depicted in Figure 2a,  $G_1$  is situated within the  $1\sigma$  region of the short-duration GRB population whereas  $G_2$  does fall within the  $1\sigma$  region of the long-duration GRB population.

### **Minimum Variability Timescale.**

The minimum variability timescale (MVT,  $\Delta t_{\min}$ ) represents the shortest observable timescale over which a GRB exhibits significant flux variations. This metric provides insights into the minimum size of the emitting region and the underlying energy dissipation physics. For long-duration GRBs (IGRBs) and short-duration GRBs (sGRBs), the median MVTs based on a Fermi burst sample

<sup>2</sup><https://heasarc.gsfc.nasa.gov/W3Browse/fermi/fermigdays.html>

are 134 ms and 18 ms, respectively (16). We determine the MVT for each individual burst of GRB 160425A by applying the technique utilizing Haar wavelets to the mask-weighted *Swift*/BAT light curve with 1 ms binning, following the procedure in Ref. (15). Our analysis reveals a MVT of  $18.5 \pm 3.1$  ms for  $G_1$  and  $550 \pm 32$  ms for  $G_2$  (Table 2 and Figure 2). This suggests that  $G_1$  is consistent with the properties of short-duration (Type-I) GRBs, while  $G_2$  aligns with the characteristics of long-duration (Type-II) GRBs.

### Amplitude Parameter.

The ‘‘amplitude’’ parameter  $f$ , defined by  $f \equiv \frac{F_p}{F_b}$ , has been proposed as a criterion to differentiate a short-duration burst serving as a ‘‘tip-of-iceberg’’ of a long-duration burst or being a genuinely short-duration burst (8), where  $F_p$  and  $F_b$  are the peak flux and average background flux of the GRB light curve, respectively. According to statistical findings based on a large *Swift* GRB sample, a disguised short-duration GRB would have  $f < 1.5$ , ref. (8). In GRB 160425A, we obtain  $f = 2.13 \pm 0.18$  for  $G_1$  (refer to Table 2 and Figure 1), a value that lies outside the range associated with disguised short-duration GRBs. This observation strongly suggests that  $G_1$  exhibits characteristics consistent with genuinely short-duration GRBs.

The tip-of-iceberg effect can disguise some long-duration Type II GRBs as apparently short-duration Type I GRBs. To distinguish intrinsically short-duration Type I GRBs, an effective amplitude parameter  $f_{\text{eff}} \equiv \frac{F'_p}{F_b} = \xi f$  can be defined for long-duration Type II GRBs by quantifying this effect. Here,  $F'_p$  is the peak flux of a pseudo-GRB with amplitude lowered by a factor  $\xi$  from an original long-duration GRB so its duration falls under 2 s. Typically, long-duration Type II GRBs have systematically smaller  $f_{\text{eff}}$  than the short-duration Type I GRBs. Following the procedure in Ref. (8), we determine  $f_{\text{eff}} = 1.05 \pm 0.03$  for  $G_2$  of GRB 160425A, as listed in Table 2. This small  $f_{\text{eff}}$  aligns with known values for long-duration GRBs.

### Spectral Lag.

Spectral lag, as defined by Norris et al. (6), refers to the time difference in the arrival of gamma-ray photons of different energies emitted during a gamma-ray burst. This phenomenon, observed in the majority of GRBs, serves as a distinguishing factor between the characteristics of long-duration and short-duration bursts. Typically, a time delay is observed between the light curves of two energy bands, with the higher energy band peaking earlier than the lower energy band. Observations show that short-duration Type-I GRBs exhibit a negligible or even negative spectral lag whereas long-duration Type-II GRBs are associated with a significant spectral lag (19, 20, 28). We use the cross-correlation function (CCF (6, 73–75)) analysis method to assess the time-averaged spectral lag and its uncertainty between the light curves of the softest band and progressively harder band for each individual burst of GRB 160425A (see Table S2 and Figure 2). The modified CCF derived

by Ref. (74), without mean-subtraction, is better suited for transient events such as GRBs. For two count rate series  $x_i$  and  $y_i$ , where  $i=0,1,2,\dots,(N-1)$ , the modified CCF can be written as

$$\text{CCF}(k\Delta t; x, y) = \frac{\sum_{i=\max(1,1-k)}^{\min(N,N-k)} x_i y_{(i+k)}}{\sqrt{\sum_i x_i^2 \sum_i y_i^2}}, \quad (\text{S3})$$

where  $\Delta t$  represents the time bin duration,  $k\Delta t$  ( $k=\dots, -1, 0, 1, \dots$ ) denotes the time delay, and  $x_i$  and  $y_i$  are the count rates in energy bands  $E_1$  and  $E_2$ .

In our analysis, we consider four standard *Swift*-BAT energy bands: 15-25 keV (channel 1), 25-50 keV (channel 2), 50-100 keV (channel 3), and 100-350 keV (channel 4). For  $G_1$ , using a 32-ms binned light curve, we calculate the spectral lag between  $T_0-0.2$  s and  $T_0+1.5$  s across these standard energy bands. For  $G_2$ , a 256-ms binned light curve is employed, and the spectral lag analysis between  $T_0+257.0$  s and  $T_0+308.02$  s is conducted. Despite obtaining non-zero spectral lags for  $G_2$ , these values are closer to those of long-duration GRBs. However, the spectral lags from  $G_1$  are notably close to zero (tiny spectral lags) and much smaller than those from  $G_2$ .

### Norris Correlation.

We measured the isotropic peak luminosity of each individual burst of GRB 160425A and overplotted the  $L_{p,\text{iso}} - \tau$  diagram (Norris relation) using a GRB sample studied in Ref. (6), and the (100-300 keV) to (25-50 keV) spectral lag is adopted. Long-duration GRBs typically align with the Norris relation, whereas short-duration GRBs tend to deviate from it. The individual bursts of GRB 160425A are denoted by colored stars in Figure 2d, while the GRB sample in Ref. (6) is represented by colored points. We observe that  $G_2$  follows the Norris relation, whereas  $G_1$  significantly deviates from it, suggesting distinct origins between  $G_1$  and  $G_2$ .

### Estimate the $E_p$ of $G_1$

Since *Swift*-BAT operates within a relatively narrow energy band (15-150 keV) in its detectors, the spectrum of  $G_1$  (-0.20 ~ 1.50) is best fitted by a simple power-law model within the BAT energy band, yielding a normalized coefficient  $A=14.6_{-3.5}^{+3.5}$  and power-law index  $\alpha=-1.75\pm 0.06$ . Consequently, the peak energy  $E_p$  of  $G_1$  must lie beyond the BAT band ( $E_p > 150$  keV).

We developed a novel approach to infer a robust lower limit on  $E_p$  when it lies beyond the instrument's upper energy threshold (76). Our procedure to estimate  $E_p$ , along with the corresponding bolometric fluence ( $S_\gamma$ ) and  $k$ -corrected ( $1-10^4$  keV) isotropic energy released in the  $\gamma$ -ray band ( $E_{\gamma,\text{iso}}$ ), involves the following steps. (1) To estimate a lower limit on  $E_p$ , we fix  $E_p$  at a sequence of values extending beyond BAT's upper limit (e.g., from 150 keV up to several MeV, Figure S5a). For each fixed  $E_p$ , we perform Markov Chain Monte Carlo (MCMC) sampling to explore the posterior distributions of the remaining free parameters ( $A$ ,  $\alpha$ , and  $\beta$ ). (2) For each fixed  $E_p$ , we compute

several statistical criteria to assess the goodness-of-fit while accounting for model complexity. We analyze how these criteria vary with the fixed  $E_p$ . As  $E_p$  increases beyond the true peak energy, improvements in fit quality diminish, resulting in a “bending point” or plateau in the criteria curves (Figure S5b). This bending point serves as a robust lower limit for  $E_p$ . To estimate the uncertainty in the  $E_p$  lower limit, we consider the spread of bending points across different criteria. The posterior distributions from MCMC sampling also provide credible intervals for  $A$ ,  $\alpha$ , and  $\beta$  at each fixed  $E_p$ , allowing us to assess parameter uncertainties comprehensively. (3) In practice, we applied this new method to estimate the lower limit for  $G_1$ . As shown in Figure S5b, the bending points in the information criteria curves were observed at  $E_p \approx 500$  keV for AIC, BIC, DIC, and  $\chi^2_\nu$ . Therefore, we used  $E_p = 500$  keV as the peak energy of  $G_1$  for the following analysis (Figure S5c).

We also utilize the full Fermi/GBM burst sample to determine a potential upper limit for  $E_p$  of  $G_1$ . This analysis incorporates a complete GBM burst sample (before May 2024) comprising 3762 bursts. We establish a separation line for  $E_p$  lying on the  $3\sigma$  region of the  $E_p$  distribution for the full Fermi/GBM burst catalog available at <https://heasarc.gsfc.nasa.gov/W3Browse/fermi/fermigbrst.html>. To accomplish this, we fit the  $E_p$  distribution for the full Fermi/GBM burst catalog with log-normal distributions,  $N(\mu, \sigma^2)$ , where  $\mu$  and  $\sigma$  represent the mean and standard deviation. The fits yield  $N_{\text{GRBs}}(2.24, 0.44^2)$  for the full GBM GRB sample. Based on these findings, we calculate the probability (denoted as  $P_{\text{GRB}}$ ) of  $G_1$  belonging to the GRB population. At a confidence level (CL) of  $3\sigma$ , we obtain  $P_{\text{GRB}} = 6.0 \times 10^{-4}$  and  $E_p = 3648$  keV. This corresponds to a CL of  $3\sigma$  and  $P_{\text{GRB}} = 6.0 \times 10^{-4}$  for rejecting the GRB population (refer to Figure S5d). In Figure S5e, we present these three distinct  $E_p$  values ( $E_p = 150$  keV, 500 keV, and 3648 keV) along with their corresponding spectral shapes, and illustrate their impact on the calculation of  $S_\gamma$  (note that  $S_\gamma$  is sensitive to the choice of  $E_p$ ), as shown on the  $E_{p,z}$ - $E_{\gamma,\text{iso}}$  diagram.

### Amati Correlation.

The correlation between the rest-frame peak energy  $E_{p,z}$  and the isotropic-bolometric-equivalent emission energy  $E_{\gamma,\text{iso}} = 4\pi d_L^2 S_\gamma k_c / (1+z)$  of GRBs was initially discovered in Ref. (21). Here,  $d_L$  represents the luminosity distance,  $S_\gamma$  denotes the energy fluence (in  $\text{erg cm}^{-2}$ ),  $k_c$  stands for the  $k$ -correction factor (adjusting the observed energy range to 1-10<sup>4</sup> keV), and  $z$  signifies the redshift. It has been used to distinguish between the properties of long-duration and short-duration bursts, as short-duration and long-duration GRBs do not conform to the same Amati relation on the  $E_{p,z}$ - $E_{\gamma,\text{iso}}$  diagram (21). By utilizing GRB samples with known redshift (4, 9, 21), we over-plotted the  $E_{p,z}$ - $E_{\gamma,\text{iso}}$  diagram (Figure S1a). The luminosity distance was calculated using the standard  $\Lambda$ -CDM cosmological parameters set with  $H_0 = 67.4 \text{ kms}^{-1} \text{ Mpc}^{-1}$ ,  $\Omega_M = 0.315$ , and  $\Omega_\Lambda = 0.685$  throughout the paper (77).

### **EH and EHD Parameters.**

Two parameters,  $\text{EH} = E_{\text{p},i,2} E_{\text{iso},51}^{-0.4}$  and  $\text{EHD} = E_{\text{p},i,2} E_{\text{iso},51}^{-0.4} T_{90,i}^{-0.5}$ , were introduced for the classification of GRBs into Type I and Type II categories (11). This classification method is particularly useful for GRBs with unknown redshifts. Here,  $E_{\text{p},i,2}$  represents the rest-frame peak energy  $E_{\text{p},i}$  in units of 100 keV,  $E_{\text{iso},51}$  denotes the isotropic equivalent energy  $E_{\gamma,\text{iso}}$  in units of  $10^{51}$  erg, and  $T_{90,i}$  stands for the rest-frame duration in seconds. The most reliable parameter for blind Type I and Type II classification, as suggested in Ref. (11), is the EHD distribution. Type I GRBs tend to cluster in the high-EHD region, while Type II GRBs are typically found in the low-EHD region, with a separation point occurring at  $\text{EHD} = 2.6$ . We calculated EHD for each of the two sub-bursts of GRB 160425A and found that  $G_1$  has  $\text{EHD} = 9.5$ , whereas  $G_2$  has  $\text{EHD} = 0.01$ . Subsequently, we compared the two bursts on the  $\text{EHD}-T_{90,i}$  diagram (see Figure S1c). As a result,  $G_1$  falls within the high-EHD region, while  $G_2$  falls within the low-EHD region.

### **$\varepsilon$ Parameter.**

By introducing the parameter  $\varepsilon = E_{\gamma,\text{iso},52} / E_{\text{p},z,2}^{5/3}$ , a phenomenological classification method was introduced to distinguish the physical origins of GRBs, distinguishing between Type I (compact star origin) and Type II (massive star origin) GRBs. The two-class GRBs tend to cluster nicely in high  $\varepsilon$  ( $\varepsilon > 0.03$ ) and low  $\varepsilon$  ( $\varepsilon < 0.03$ ) regions, respectively, with a separation line at  $\varepsilon \sim 0.03$  using a GRB sample with known redshift (7). We calculated  $\varepsilon$  for each individual burst of GRB 160425A and compared them on the  $\log \varepsilon - \log t_{90,z}$  plane. It was observed that  $G_1$  falls within the low- $\varepsilon$  region, while  $G_2$  falls within the high- $\varepsilon$  region (Figure S1d). These results suggest that  $G_1$  is likely of a Type I origin, whereas  $G_2$  should be of a Type II origin.

### **Swift-XRT Afterglow Light Curves.**

Short-duration GRBs are known to exhibit lower luminosity compared to typical long-duration GRBs in their afterglow light curve observed by *Swift*-XRT data (47). To differentiate the afterglow properties of GRB 160425A between short-duration and long-duration GRB populations, a sample of 248 GRBs (217 long-duration GRBs and 31 short-duration GRBs) observed by *Swift*-XRT with known redshift from 2004 to 2015 was compiled (44–46). Using this sample, we over-plotted the luminosity as a function of rest-frame time on the  $L_{\text{AG,iso}} - t_z$  diagram (Figure S2a), where  $L_{\text{AG,iso}}$  is the luminosity of the X-ray afterglow and  $t_z = t/(1+z)$  is the rest-frame time. In the diagram, GRB 160425A is indicated by yellow data points, while the GRB sample is depicted by black and grey lines for short-duration (Type I) and long-duration (Type II) GRB populations, respectively. Notably, GRB 160425A appears at the bottom edge region of the long-burst distribution, but at the top edge region of the short-burst distribution. These results suggest that we cannot definitively classify GRB 160425A as either a Type I or Type II  $\gamma$ -ray burst based solely on its afterglow

emission.

### **X-ray Afterglow Observations.**

The *Swift* X-ray Telescope (XRT) began to observe the BAT field from 208 s to 1171 ks after the BAT trigger. It identified a fading, uncatalogued X-ray source with an enhanced position located at RA=18h41m18.56s and DEC=-54°21'36.2'' (J2000) with an uncertainty of 2.0''. The initial data was obtained in 439 s in Window Timing (WT) mode with the remainder in Photon Counting (PC) mode. The X-ray light curve of GRB 160425A exhibits two distinct phases: an early-time X-ray flare and a late-time normal decay. We fit the X-ray flare (from 208 and  $\sim 600$  s) with a smooth broken power-law model. The best-fit parameters give  $\alpha_1 = -43.90 \pm 3.91$ ,  $\alpha_2 = 6.06 \pm 0.21$ , and  $t_p = 270 \pm 45$  s. The following normal decay (between  $\sim 600$  s and 1171 ks) can be modeled with a power-law decay with a power-law index  $\alpha_X = -1.03 \pm 0.06$ . The results suggest that the early X-ray flare is consistent with the activation of the central engine, whereas the subsequent normal decay phase aligns with the standard external shock afterglow model. These light curve fits are performed using the *lmfitt* (78), employing a nonlinear least-squares method with the Levenberg-Marquardt minimization algorithm to fit the data. The convention  $F_\nu \propto t^{-\alpha_X} \nu^{-\beta_X}$  is adopted, where  $\alpha_X$  represents the temporal index of the light curve, and  $\beta_X$  is the photon index of the X-ray spectrum, with  $\beta_X = \Gamma_X - 1$ .

### **Ultraviolet (UV)/Optical, and Near-Infrared Afterglow Observations.**

At the coordinates provided by *Swift*-XRT, we gathered ultraviolet, optical, and near-infrared observations (see Table S5). Optical data were either obtained from GCN circulars (<https://gcn.gsfc.nasa.gov/other/160425A.gcn3>) by multiple facilities (ESO-2.2m MPG and CTIO-1.3m ANDICAM) or by the *Swift* Ultraviolet and Optical Telescope (UVOT (79)) from the *Swift* archive website (<https://www.swift.ac.uk/archive/q1.php>) (Table S5), together with our own observations performed by the Gamma-Ray Burst Optical/Near-Infrared Detector (GROND), attached to the MPG/ESO 2.2-metre telescope at La Silla Observatory (Table S6). To account for host galaxy and Galactic extinctions, as well as spectral  $k$ -corrections, corrections were applied to the observed data. Galactic extinction correction utilized the reddening map presented in (80) for optical and near-IR magnitudes. The  $k$ -correction was applied to the observed spectra, defined as  $m_T = m_O - k$ , following refs. (81, 82), with  $k = 2.5(\beta_o - 1) \log(1 + z)$ , where  $m_O$  and  $m_T$  are the observed and true magnitudes, respectively,  $\beta_o$  is the spectral index measured from the optical afterglow (a typical value  $\beta_o=0.75$  is applied), and  $z$  is the redshift. Using a typical  $A_V$  value ( $\log_{10} A_V^{\text{host}} = -0.82 \pm 0.41$ , see Figure 1 in ref. (83)) and assuming  $R_V=3.1$ , the host extinction correction in any optical band,  $A_\lambda$ , was calculated following the extinction curve defined in ref. (84),

where  $R_V \equiv A_V/E_{B-V}$  is the total-to-selective extinction ratio, and the color excess  $E_{B-V} \equiv A_B - A_V$  represents the difference between the extinction in B and V filters.

### Unable to Determine Supernova.

The observation of supernovae association is one of the most confident pieces of evidence for the progenitor of a GRB. It is generally accepted that Type I bursts are formed by the merger of binary compact stars without the presence of a supernova component. Type II bursts are generated by the collapse of massive stars, with nickel in their outward expanding shells releasing energetic photons through nuclear radioactive decay (47). These energetic photons are converted to optical emission escaping the opaque shells through diffusion for about two weeks (85). Hence, the determination of the supernova component which appears as a bump on the optical light curve gives a possible judgment on the Type II burst.

GRB 160425A has extremely limited optical data observations, with the majority of bands having only a single time bin. The *Swift* observations of the U band that we heavily rely on have values in two-time bins and some time bins of upper limits. U band is the best optical observational band available. It is essential to apply extinction corrections and subtract the host galaxy's background luminosity. The host galaxy of GRB 160425A has been localized, with observations from telescopes such as CTIO, MASTER and VLT (86). VLT/FORS reveals three distinct diffuse knots, suggesting a merging-galaxy system, see figure 3. Despite these observations, the U-band magnitude of the host galaxy remains unavailable. Late-time CTIO observations report an I-band magnitude of 20.1, with no significant brightness variation (uncertainty  $< 0.05$  mag) between 7 and 26 days post-burst. A supernova similar to SN 1998bw would have brightened the I-band by 0.1 magnitudes, which was not observed. These findings lead to the conclusion that if this is a long-duration GRB, any associated supernova must be dimmer than SN 1998bw. For typical star formation galaxies, the magnitude of  $U - I$  is around 1.0 to 2.0 (87), hence we assume the galaxy's U-band brightness ( $\sim 21.6 \pm 0.5$  mag), the corresponding flux density is approximately 0.008 mJy, which is close to the observed U-band flux density. This means after subtracting the host galaxy's contribution, the U-band flux would be very faint, as shown in Fig. S4. Due to the uncertainty in the brightness of the host galaxy, the error in the U-band data points has increased, particularly for the last data point, where the minimum value has already fallen below the flux of synchrotron radiation. Therefore, it is likely the last point is from the host galaxy, not mainly contributed from the GRB. This makes it impossible to determine whether there is a supernova component present.

Though it is uncertain, we still adopt SN 1998bw as a template light curve (88) trying to limit the SN component by adjusting the redshift and scaling the luminosity and time (89). We obtain the quasi-bolometric unreddened rest-frame light curves of SN 1998bw from Ref. (88). To generate a particular supernova light curve, we apply a scaling factor,  $k$ , and a stretch factor,  $s$ , to the template supernova, SN 1998bw. At redshift  $z$ , the observed flux density of the specific supernova can be

given by:

$$F_{\nu}^{\text{SN}}(t_{\text{obs}}, \nu_{\text{obs}}) = \frac{(1+z)k}{4\pi d_L^2} L_{\nu}^{\text{SN}} \left( \frac{t_{\text{obs}}}{(1+z)s}, (1+z)\nu_{\text{obs}} \right) \quad (\text{S4})$$

where  $d_L$  is luminosity distance and  $L_{\nu}^{\text{SN}}$  is specific luminosity at frequency  $\nu$  of template supernova. In order to obtain plausible results from the limited data, we use numerical simulations of the forward shockwave model to derive the synchrotron component of the afterglow (90). In Figure S4, we present the multi-wavelength observations of GRB 160425A alongside the fitted Gaussian jet model. Parameters include isotropic-equivalent energy of the jet set to  $E_0 = 0.9 \times 10^{53}$  erg. The circumburst medium density is  $n_0 = 0.001 \text{ cm}^{-3}$ , and the electron energy distribution index is  $p = 2.15$ . The microphysical parameters are  $\epsilon_e = 0.28$  and  $\epsilon_B = 0.001$ . To estimate the maximum luminosity of a hypothetical supernova under the constraints of the data, we found  $s = 0.9$  and  $k = 1$ . This indicates that, if a supernova is present, its upper-limit brightness is at least one magnitude fainter than that of SN 1998bw. This result is consistent with the aforementioned CTIO observations.

We conclude that the data is insufficient to confirm the existence of a supernova, suggesting there is either no supernova component or a very weak one.

### The BAT-determined Position of $G_1$ and $G_2$ .

We adopt the HEASoft tools `batbinevt`, `batfftimage`, and `batcelldetect`, which analyze the event file, generate images, and derive source positions for each of the spikes. For the first spike  $G_1$ , we determined the centroid to be at RA = 280.34 ° and DEC = -54.36°, the positional error is 0.02°. For the second spike  $G_2$ , we determined the centroid to be at RA = 280.29° and DEC = -54.35°, the error is 0.02°. To check if the two spikes share the same origin, we then compute the angular separation between the centroids and the combined positional error. The angular separation is 0.03° or about 1.69 arcminutes. The combined positional error is 0.02° or 1.42 arcminutes. Our results show that the positions of the two spikes are consistent within the uncertainties. We conclude that the two emission episodes in GRB 160425A likely come from the same astrophysical source.

### Host Galaxy Observations and Properties.

It is imperative to consider the properties of the host galaxy when endeavoring to classify GRBs from a physical standpoint. Analysis of emission lines such as H $\alpha$ , H $\beta$ , [O III], [O II], and [S III], the spectrum indicates two different systems at  $z=0.555$ . The observed velocity separation amounts to 180 km/s, while the spatial separation aligns with the three knots visible in the imaging (corresponding to 8 kpcs at this distance), indicating an interacting pair of galaxies (86).

*Spectrum.* The host galaxy of GRB 160425A has been observed with VLT/X-shooter on 2016 April 26, as part of the XSGRB project (91). The reduced spectrum is available in <https://>

//sid.erda.dk/share\\_redirect/DBuNORk11I/XSGRB.zip in the standard ESO format. We fit the emission lines with the GLEAM (92). It turns out that the  $H\alpha$  flux is  $(0.8 \pm 0.2) \times 10^{-16}$  ergs/s/cm<sup>2</sup>. After correcting the Milky Way extinction (93), the luminosity is  $(1.1 \pm 0.3) \times 10^{41}$  erg/s. Although the spectrum must be a combination of the afterglow and the host galaxy, the continuum is dominated by the afterglow, and the emission lines are expected to be dominated by the host galaxy. Considering the possible contamination of the afterglow, we should consider the uncertainty of SFR as a lower limit. With the  $H\alpha$  luminosity, the star formation rate (SFR) of the host galaxy is estimated to be  $\text{SFR} = L_{H\alpha}/1.86 \times 10^{41} M_{\odot} \text{ yr}^{-1} = 0.58 M_{\odot} \text{ yr}^{-1}$  (94). We estimate the metallicity with  $12 + \log(\text{O}/\text{H}) = 8.73 - 0.32 \times \text{O3N2}$ , where  $\text{O3N2} = \log\{([\text{OIII}]\lambda 5007/\text{H}\beta)/([\text{NII}]\lambda 6583/\text{H}\alpha)\}$  (95). It turns out to be 8.53, a metal poorer than solar metallicity.

*Image.* The image of GRB 160425A has been taken with VLT/FORS2 many times during 2016 May 13th to 2016 September 3rd. To analyze the host galaxy properties, we only use the images of September 3rd 2016 to eliminate the contamination of the afterglow. We use the *EsoReflex* (96)<sup>3</sup> to subtract bias and sky flat field. After detecting objects with *SExtractor* (97)<sup>4</sup>, we register the images with *SCAMP* (98)<sup>5</sup>, and resample the images with *SWARP* (99)<sup>6</sup> for a pixel scale 0.125". The image of the host galaxy is presented as panels of Figure 3. We registered the Swift/UVOT white band image observed on April 25 2016 to the GAIA/DR2 catalog and detected the afterglow to be 18:41:18.5562, -54:21:36.416. After registering the VLT/FORS image to the Swift/UVOT image, the center of the host galaxy was detected as 18:41:18.5247, -54:21:36.334. Thus, the offset from the afterglow to the center of the host is 0.29", corresponding to  $R_{\text{off}} = 1.86$  kpc. We fit the galaxy with *GALFIT*<sup>7</sup>. It turns out that  $R_{50}$  is 0.39", which is 2.5 kpc at redshift 0.555. The normalized offset  $r_{\text{off}} = R_{\text{off}}/R_{50} = 0.7$ , where  $R_{50}$  is the half-light radius. The cumulative light fraction  $F_{\text{light}} \sim 0.6$ .

To assess the probability that GRB 160425A belongs to the short-duration or long-duration GRB population, we compare its host galaxy properties with the corresponding parameter distributions constructed from a large catalog of GRB host galaxy data (10, 100).

*Redshift.* We compiled a complete sample of 565 GRBs with measured redshift from a variety multi-mission observations. This sample comprises 485 long-duration GRBs and 78 short-duration GRBs. To characterize the redshift distributions of these two distinct GRB populations, we independently fitted each with a single log-normal function,  $N(\mu, \sigma^2)$ , where  $\mu$  and  $\sigma$  represent the mean and standard deviation, all in logarithmic space. For sGRBs, the best fit yielded  $N_{\text{sGRBs}}(-0.08, 0.33^2)$ , while for IGRBs, the distribution was found to be  $N_{\text{IGRBs}}(0.24, 0.31^2)$ . Based on these derived distributions, we evaluated the probability of observing a GRB at a specific redshift. The  $p$ -values

<sup>3</sup><https://www.eso.org/sci/software/esoreflex/>

<sup>4</sup><https://www.astromatic.net/software/sextractor/>

<sup>5</sup><https://www.astromatic.net/software/scamp/>

<sup>6</sup><https://www.astromatic.net/software/swarp/>

<sup>7</sup><https://users.obs.carnegiescience.edu/peng/work/galfit/galfit.html>

corresponding to  $z = 0.555$  for GRB 160425A are 0.29 from the sGRB population and 0.05 from the lGRB population. This implies that GRB 160425A is rejected from being a short-duration GRB with a confidence level of  $0.54\sigma$  and a long-duration GRB with a confidence level of  $1.63\sigma$ , respectively. Consequently, GRB 160425A, with a redshift of 0.555, is more consistent with a typical short-duration (Type I) GRB (Table S4 and Figure S6a).

*SFR.* To further assess the classification, we investigated its association with star formation rate (SFR), a key property influencing GRB progenitors. We compared its properties with a comprehensive GRB sample from Ref. (10), which includes 183 long-duration GRBs and 19 short-duration GRBs. We modeled the SFR distributions for both distributions using a single log-normal function. For short-duration GRBs, the distributions was  $N_{\text{sGRBs}}(0.83, 1.14^2)$ , while for long-duration GRBs, it was  $N_{\text{lGRBs}}(0.76, 0.84^2)$ . These fits allow us to quantify the likelihood of a GRB belonging to either population based its SFR. GRB 160425A exhibits an SFR of  $0.58 M_{\odot} \text{ yr}^{-1}$ . Based on our fitted distributions, the corresponding  $p$ -values are 0.18 from the sGRB population and 0.12 from the lGRB population. This implies that GRB 160425A is rejected from being a short-duration GRB with a confidence level of  $0.93\sigma$  and a long-duration GRB with a confidence level of  $1.18\sigma$ , respectively. Consequently, GRB 160425A, with an SFR of  $0.58 M_{\odot} \text{ yr}^{-1}$ , is favored as a typical short-duration GRB (see Table S4 and Figure S6b).

*$R_{\text{off}}$ .* To establish a robust statistical sample for  $R_{\text{off}}$  analysis, we compiled a comprehensive dataset of GRB offsets by combining data from Ref. (10, 100). The Ref. (10) sample provided 132 long-duration GRB with precisely measured offset (excluding any upper or lower limits). However, it only included 25 short-duration GRBs with similarly robust offset measurements. To significantly enhance the short-duration GRB statistics, we incorporated an updated and more complete short-duration GRB sample from Ref. (100), which contributed an additional 83 short-duration GRBs with precisely measured offsets. We modeled the  $R_{\text{off}}$  distributions for both GRB populations using a single log-normal function. For sGRBs, the best fit yielded  $N_{\text{sGRBs}}(0.91, 0.68^2)$ , which for lGRBs, the distribution was found to be  $N_{\text{lGRBs}}(0.29, 0.62^2)$ . These fits allow us to quantify the likelihood of a GRB belonging to either population based its measured  $R_{\text{off}}$ . GRB 160425A exhibits an  $R_{\text{off}}$  of 1.86 kpc. Based on our fitted distributions, the corresponding  $p$ -values are 0.17 from the sGRB population and 0.49 from the lGRB population. This implies that GRB 160425A is rejected from being a short-duration GRB with a confidence level of  $0.94\sigma$  and a long-duration GRB with a confidence level of  $0.03\sigma$ , respectively. Consequently, GRB 160425A, with an  $R_{\text{off}}$  of 1.86 kpc, is far more consistent with a long-duration GRB (Table S4 and Figure S6c).

*$R_{50}$ .* We compiled a comprehensive dataset of GRB  $R_{50}$  values from Ref. (10). This sample comprises 124 long-duration GRBs and 24 short-duration GRBs, all with precisely measured  $R_{50}$  values. We modeled both distribution using a single log-normal function. For sGRBs, the fitted distribution was  $N_{\text{sGRBs}}(0.27, 0.40^2)$ , while for long-duration GRBs, it was  $N_{\text{lGRBs}}(0.27, 0.30^2)$ . These fits enable us to quantify the likelihood of a GRB belonging to either population based its

measured  $R_{50}$ . GRB 160425A exhibits an  $R_{50}$  of 2.5 kpc. Based on our fitted distributions, the corresponding  $p$ -values are 0.63 from the sGRB population and 0.66 from the lGRB population. This implies that GRB 160425A is rejected from being a short-duration GRB with a confidence level of  $0.32\sigma$  and a long-duration GRB with a confidence level of  $0.41\sigma$ , respectively. Consequently, GRB 160425A, with an  $R_{50}$  of 2.5 kpc, is more consistent with a short-duration (Type I) GRB (Table S4 and Figure S6d).

$r_{\text{off}}$ . We constructed a complete catalog of GRB normalized offset ( $R_{\text{off}}$ ) using data from Ref. (10). This final sample comprises 118 long-duration GRBs and 23 short-duration GRBs, each with robust  $r_{\text{off}}$  measurement free of upper or lower limits. We modeled both distributions using a single log-normal function. For sGRBs, the distribution was  $N_{\text{sGRBs}}(0.29, 0.62^2)$ , while for lGRBs, it was  $N_{\text{lGRBs}}(0.91, 0.68^2)$  for short-duration GRBs. These fits allow us to quantify the likelihood of a GRB belonging to either population based its measured  $r_{\text{off}}$ . GRB 160425A exhibits an  $r_{\text{off}}$  of 0.7. Based on our fitted distributions, the corresponding  $p$ -values are 0.27 from the sGRB population and 0.41 from the lGRB population. This implies that GRB 160425A is rejected from being a short-duration GRB with a confidence level of  $0.62\sigma$  and a long-duration GRB with a confidence level of  $0.41\sigma$ , respectively. Consequently, GRB 160425A, with an  $r_{\text{off}}$  of 0.7, is more consistent with a long-duration (Type II) GRB (Table S4 and Figure S6e).

$F_{\text{light}}$ . We assembled a comprehensive dataset of GRB  $F_{\text{light}}$  using the catalog from Ref. (10). This final sample contains 99 long-duration GRBs and 20 short-duration GRBs, all with accurately determined  $F_{\text{light}}$  values unaffected by upper or lower limits. Initially, we attempted to model both distributions using a single normal function. However, this approach proved unsuccessful, as the fitted parameters can not be well-constrained. Consequently, we employed a Kernel Density Estimation (KDE) function to assess the likelihood of GRB 160425A belonging to either the short-duration or long-duration GRB populations. At an  $F_{\text{light}}$  value of approximately 0.6, we obtained a KDE probability density of 0.57 for short-duration GRB population and 0.86 for the long-duration GRB population. These results suggest that GRB 160425A is more consistent with a long-duration (Type II) GRB (Table S4 and Figure S6f).

## **GRB 160425A in Synchrotron Afterglow Emissions of *Swift* GRBs**

We compare the afterglow synchrotron parameters of GRB 160425A with other GRBs.

We constructed a sample of Swift–XRT gamma-ray bursts (GRBs) with known redshift. Light curves were retrieved from the UK Swift Science Data Centre and included both Windowed Timing and Photon Counting modes. We excluded incomplete light curves that had no observations before 1000 s, and also excluded those with fewer than 10 data points in the default binning on the UKSSDC website. In total, 147 GRBs are selected. Early-time flares and late-time bumps were excluded to isolate the forward-shock afterglow emission. To improve the homogeneity of the dataset and reduce statistical imbalance at late times, we applied a logarithmic rebinning in observer time. The

observed 0.3–10 keV fluxes were converted into monochromatic flux density at 1 keV, assuming a power-law photon spectrum.

The afterglow emission was modeled with a semi-analytic synchrotron forward-shock code, `jetsimpy`, which computes broadband light curves for both constant-density interstellar medium (ISM) and stellar wind density profiles. The physical parameters of interest included the isotropic-equivalent kinetic energy  $E_{\text{iso}}$ , initial Lorentz factor  $\Gamma_0$ , circumburst density  $n_{\text{env}}$ , electron energy fraction  $\epsilon_e$ , magnetic energy fraction  $\epsilon_B$ , and electron power-law index  $p$ . Log-uniform priors were adopted for energy and microphysical fractions, and uniform priors for  $p$ . Posterior distributions were obtained using the affine-invariant MCMC sampler `emcee`, with convergence monitored via autocorrelation analysis. To assess the circumburst environment, we compared ISM and wind fits using the Deviance Information Criterion (DIC), with  $\Delta\text{DIC} \gtrsim 5$  considered substantial evidence.

The derived distributions reveal commonalities and systematic differences between short-duration and long-duration GRBs. The electron energy fraction clusters tightly around  $\epsilon_e \approx 0.2\text{--}0.3$ , with long-duration GRBs showing values modestly higher than short-duration bursts. The electron power-law index is stable across the sample, with  $p \approx 2.2\text{--}2.3$ , consistent with relativistic shock acceleration theory. In contrast, the magnetic energy fraction spans several orders of magnitude,  $\epsilon_B \sim 10^{-4}\text{--}10^{-1}$ , with medians of a few  $\times 10^{-3}$ . This wide dispersion suggests variable efficiency in magnetic field amplification.

Energetics differ strongly between populations: long-duration GRBs typically exhibit  $E_{\text{iso}} \sim 10^{52}\text{--}10^{54}$  erg, while short-duration GRBs cluster near  $5 \times 10^{51}$  erg, with no event exceeding  $2 \times 10^{52}$  erg. The latter is comparable to the maximal spin-down energy of a millisecond magnetar, indicating a natural ceiling on the afterglow energy budget. The initial Lorentz factors also separate the two populations: short-duration GRBs peak at  $\Gamma_0 \sim 300\text{--}400$ , exceeding the typical values of long-duration GRBs ( $\Gamma_0 \sim 120\text{--}250$ ). Finally, model comparison favors a constant-density ISM profile for the majority of bursts, though approximately 15% show preference for wind-like environments. Together, these results indicate that while the microphysics of shock acceleration is universal across GRB classes, their energetics, Lorentz factors, and environments reveal clear differences tied to progenitor type and central engine.

The afterglow modeling of GRB 160425A (Table S3 and Figure S3) reveals physical parameters that differ significantly from the typical distributions of long-duration and short-duration GRBs. Its isotropic-equivalent energy,  $E_{\text{iso}} \approx 3 \times 10^{52}$  erg, is consistent with the lower end of the long-duration GRB population but well above the median value for short-duration bursts ( $\sim 3 \times 10^{51}$  erg). The electron energy fraction is unusually large,  $\epsilon_e \approx 0.62$ , compared to the canonical range of 0.2–0.3 for both long-duration and short-duration GRBs. The magnetic energy fraction,  $\epsilon_B \sim 10^{-3}$ , and electron spectral index,  $p = 2.18$ , fall within the distributions expected from the broader sample. However, GRB 160425A shows an exceptionally high initial Lorentz factor,  $\Gamma_0 \sim 950$ , far exceeding the median values for long-duration ( $\sim 250$ ) and short-duration ( $\sim 420$ ) GRBs. In addition, the

circumburst density is very low,  $n_0 \sim 1.6 \times 10^{-3} \text{ cm}^{-3}$ , at least two orders of magnitude below the typical values of  $\sim 0.3 \text{ cm}^{-3}$ . These properties suggest that GRB 160425A was produced by a relativistic outflow of unusually high velocity expanding into a tenuous environment, placing it at the extreme end of the observed GRB parameter space.

### **Probability of Observing (On the Earth) Two Isolated GRBs within 250 Seconds from Two Different Galaxies at the Same Location.**

We use the following steps to estimate the probability of observing two GRBs at the same location. First, considering that the average detection rate of GRBs is 2-3 per day, we assume an average rate ( $\lambda$ ) of 2.5 GRBs per day. Converting this to an observational rate per second, we have:

$$\lambda = \frac{2.5 \text{ GRBs}}{86400 \text{ seconds}} \approx 2.89 \times 10^{-5} \text{ GRBs/second.} \quad (\text{S5})$$

Second, the probability  $P(k; \lambda T)$  of observing events ( $k$ ) in a time interval ( $T$ ) based on the Poisson distribution is given by:

$$P(k; \lambda T) = \frac{(\lambda T)^k e^{-\lambda T}}{k!}. \quad (\text{S6})$$

For  $k=2$  and  $T=250$  seconds in our case, one has:

$$\lambda T = 2.89 \times 10^{-5} \times 250 = 0.007225. \quad (\text{S7})$$

Thus, the probability of observing two GRBs in this interval can be written as:

$$P(2; 0.007225) = \frac{(0.007225)^2 e^{-0.007225}}{2!} \approx 2.59 \times 10^{-5}. \quad (\text{S8})$$

Third, using the median value of the BAT 90% error radius (1.5 arcminutes) from the *Swift* catalogue<sup>8</sup>, we can estimate a positional accuracy consideration. Converting this to degrees:

$$1.5 \text{ arcminutes} = \frac{1.5}{60} \text{ degrees} = 0.025 \text{ degrees.} \quad (\text{S9})$$

Assuming a uniform distribution over the celestial sphere, the fraction of the sky covered by a circle with a radius of 0.025 degrees (in steradians) is:

$$\left( \frac{0.025 \text{ degrees}}{180 \text{ degrees}} \cdot \pi \right)^2 \approx \left( \frac{0.025}{180} \cdot \pi \right)^2 \approx 7.62 \times 10^{-8}. \quad (\text{S10})$$

Hence, the probability that two GRBs are observed within this positional accuracy is  $7.62 \times 10^{-8}$ . Therefore, the combined probability of both events (two GRBs within 250 seconds and within 0.025-degree positional accuracy) is the product of the two independent probabilities:

$$P(2 \text{ GRBs in 250 seconds and same position}) = 2.59 \times 10^{-5} \times 7.62 \times 10^{-8} \approx 1.97 \times 10^{-12}. \quad (\text{S11})$$

<sup>8</sup>[https://www.swift.ac.uk/xrt\\_live\\_cat/](https://www.swift.ac.uk/xrt_live_cat/)

### Probability of Observing (On the Earth) Two Isolated GRBs within 250 Seconds from the Same Galaxy.

The GRB occurrence rate is given as 0.1 – 1 per million years per galaxy. Thus, the occurrence rate  $R$  of GRBs per galaxy in seconds is

$$R = 3.16 \times 10^{-15} - 3.16 \times 10^{-14} \text{ GRBs per second per galaxy.} \quad (\text{S12})$$

For a Poisson process, the probability of observing  $k$  events in a time interval  $T$  is given by

$$P(k; R \cdot T) = \frac{(R \cdot T)^k e^{-R \cdot T}}{k!}. \quad (\text{S13})$$

The probability of having two GRBs ( $k = 2$ ) occurring in the same galaxy within a 250-second interval ( $T = 250$ ) at a given time with the occurrence rate ( $R$ ) is therefore approximately

$$3.12 \times 10^{-25} - 3.12 \times 10^{-23}. \quad (\text{S14})$$

This exceedingly low probability suggests that such an occurrence is practically impossible.

If we assume that one GRB has already occurred in a given galaxy, then we compute the probability that the next GRB in the same galaxy will occur within 250 seconds. For a Poisson process with a rate  $R$ , the waiting time for the next event follows an exponential distribution, the probability that another GRB will occur in the same galaxy within 250 seconds is approximately

$$P(\text{next event within } T) = 1 - e^{-RT} \approx 7.9 \times 10^{-13} - 7.9 \times 10^{-12}, \quad (\text{S15})$$

which is on the order of  $10^{-12}$ . This probability is very small, indicating that it is extremely unlikely to see another GRB from the same galaxy within such a short time interval once one GRB has already been observed.

### Uniqueness of GRB 160425A in the Peculiar GRB Population.

Peculiar GRBs reported to date fall into two broad observational groups based on light-curve morphology. The first comprises non-quiet, continuous-emission outliers (upper panel of Table 3), including merger-like events with anomalously long  $T_{90}$  (e.g., GRB 060614 (29–31), GRB 211211A (32–34), and GRB 230307A (35, 36)), a collapsar-like event with anomalously short  $T_{90}$  (e.g., GRB 200826A (37)), and boundary cases near the short/long classification overlap (e.g., GRB 180418A (60)). Although these bursts defy duration-based classification, each constitutes a single, uninterrupted prompt-emission episode. GRB 160425A is observationally distinct: its two discrete emission episodes, separated by a significantly background-consistent quiet gap, firmly place it in the “quiet” GRB class (Figure 1).

The second group comprises quiescent, multi-episode bursts (lower panel of Table 3). A number of quiescent GRBs have been reported, attracting attention due to their prolonged quiescent periods (*101, 102*) or distinct properties between emission episodes (*50, 103*). Observationally, long-duration GRB with an early precursor in which both separated components (sub-burst) are prompt-like emission and remain long-like (e.g., GRB 060124 (*69*) and many other events (*38*)); short-duration GRB followed by a soft extended-emission tail whose post-gap component is not a conventional long-like prompt burst (e.g., GRB 050709 and related events (*18*)); double-main or double-trigger long-duration GRBs in which both separated sub-bursts are long-like (e.g., GRB 091024A (*101*), GRB 110709B (*62*), and GRB 220627A (*102, 104*)); long-duration or short-duration GRB followed by bright X-ray flares (e.g., GRB 050502B (*41*) and GRB 050724 (*42*)); and pre-quiescent long-duration GRB whose post-gap emission is more naturally interpreted as afterglow onset (e.g., GRB 960530 and GRB 980125 (*43*)). Across all of these cases, either both separated components share a common prompt-emission class, or the post-gap component is not a second genuine prompt emission burst. This pattern is reinforced by recent large-sample analyses showing that prompt-emission classification is internally consistent across all sub-burst episodes (precursor, main, extended, and double-main/trigger) within individual GRB events (*38–40*).

GRB 160425A satisfies none of the above precedents. Its two prompt-like episodes are separated by a  $\sim 256$  s background-consistent gap, yet their empirical classifications are opposite:  $G_1$  is short-like and  $G_2$  is long-like. No previously reported event combines these three properties. Continuous-emission outliers lack a separated prompt pair; previously reported quiescent bursts either preserve a common prompt-emission class across the gap or contain a post-gap component better attributed to extended emission, a flare, or afterglow onset. GRB 160425A is therefore observationally unique among known peculiar GRBs.

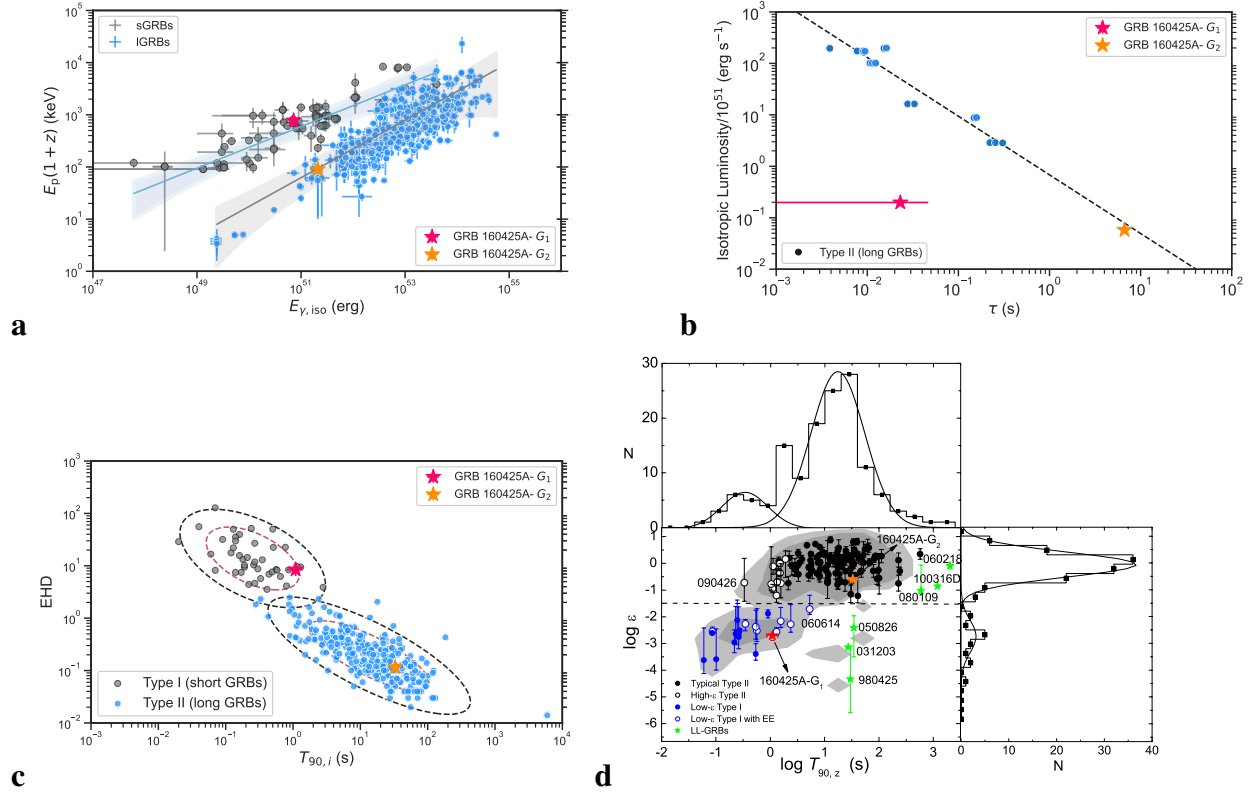


**Figure S1: Same as Figure 2, but for alternative traditional GRB classification schemes based on spectral peak energy ( $E_p$ ). a-d illustrate the  $E_p$ -related classification using the Amati relation (a), the Norris relation (b), the duration/EHD diagram (c), and the duration/ $\xi$  diagram (d). For c, d, durations are given in the source (rest) frame.**

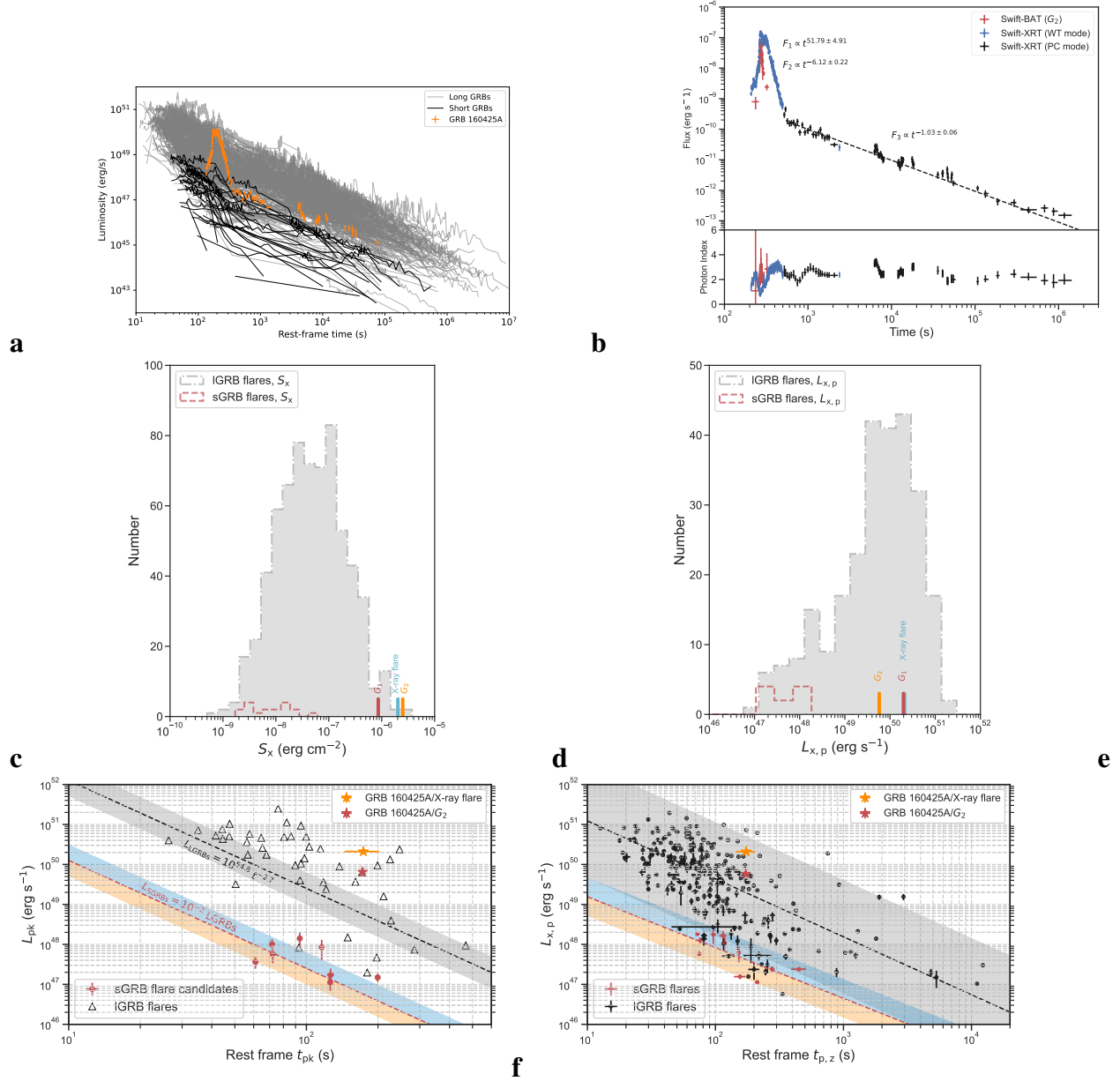


**Figure S2: *Swift*-XRT afterglow emission observations of GRB 160425A.** **a**, The XRT luminosity as a function of rest-frame time for short-duration (black) and long-duration (gray) GRBs, based on a GRB sample detected from 2004 to 2015, with GRB 160425A indicated by orange data points. **b**, X-ray light curve and photon index evolution of GRB 160425A, as well as the best-fitting of the X-ray flare and normal decay phase. **c-d**, The distributions of energy fluence ( $S_X$ ) and peak luminosity ( $L_{X,p}$ ) for XRT flares in short-duration (red) and long-duration (grey) GRBs, based on a comprehensive catalog of short-duration GRB flares and long-duration GRB flares (105). The position of  $G_1$  and  $G_2$  of GRB 160425A and its X-ray flare in the distributions is marked by red, orange, and cyan vertical cylinders, respectively. **e**, The luminosity of XRT flares as a function of rest-frame time for short-duration (red) and long-duration (grey) GRBs as well as their best model fittings (dashed lines) and  $2\sigma$  regions (shaded areas), derived from a catalog of short-duration GRB flares (49) and long-duration GRB flares (106). The X-ray flare and  $G_2$  of GRB 160425A are highlighted by orange (the X-ray flare) and red ( $G_2$ ) stars, respectively. **f**, The same as **e**, but for a different XRT flare catalog (105).

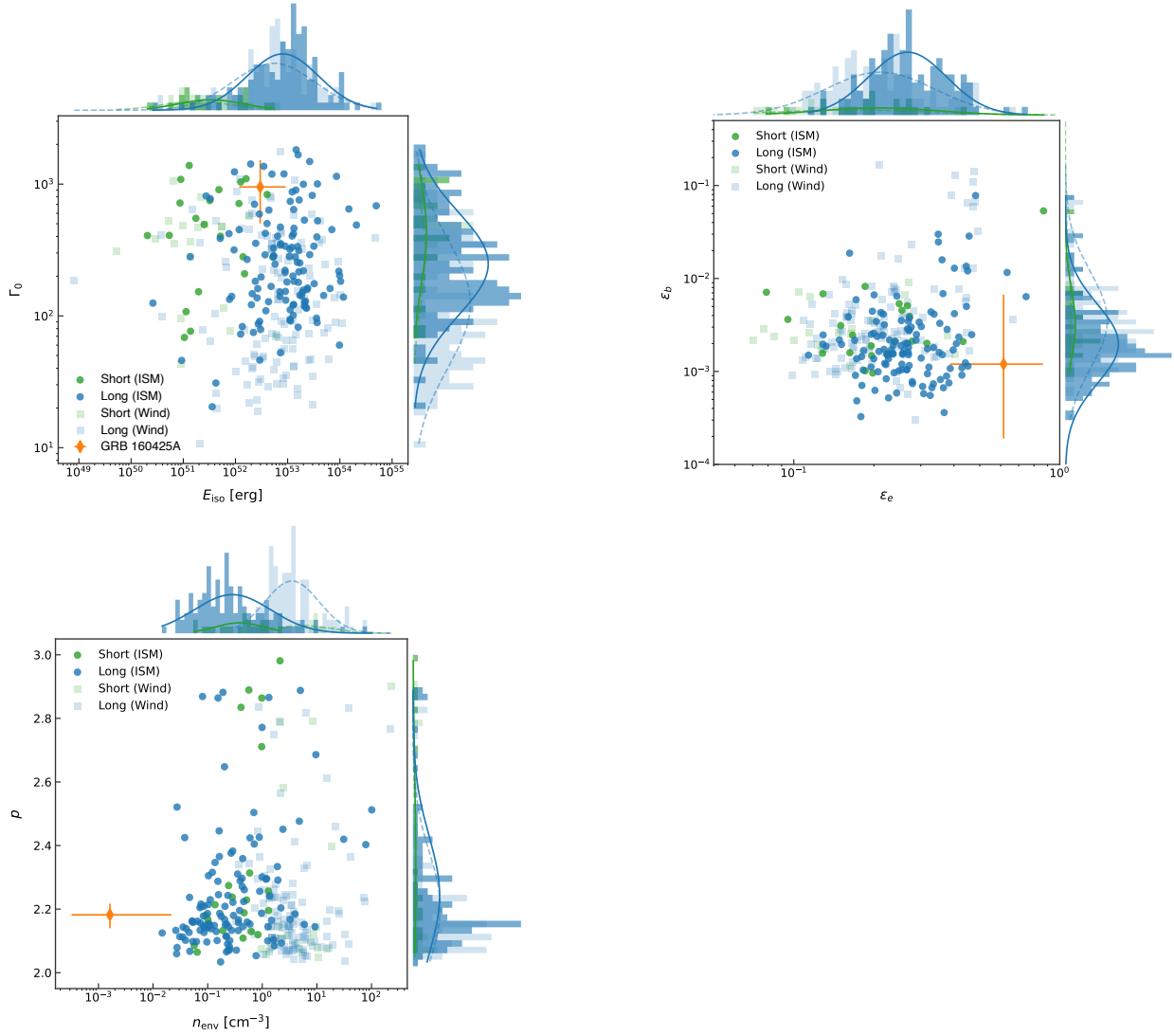


**Figure S3: GRB 160425A in synchrotron afterglow modeling of Swift GRBs.** **a**, The relationship between the isotropic equivalent energy,  $E_{\text{iso}}$ , and the initial Lorentz factor,  $\Gamma_0$ . The data is distinguished by burst class (Short-duration and long-duration GRBs) and by the assumed circumstellar medium model (ISM and Wind). The central panel displays a log-log scatter plot of  $E_{\text{iso}}$  versus  $\Gamma_0$ . The top and right panels show the corresponding distributions of these parameters as histograms. The values for GRB 160425A are shown with an error bar. **b**, The median values of the microphysical parameters,  $\epsilon_e$  (electron energy fraction) and  $\epsilon_b$  (magnetic field energy fraction). The data points are differentiated by burst class (Short-duration and long-duration GRBs) and circumstellar medium model (ISM and Wind). The central panel is a log-log scatter plot of  $\epsilon_e$  versus  $\epsilon_b$ . The top and right panels show the distributions of  $\epsilon_e$  and  $\epsilon_b$ , respectively, as histograms. Overlaid on the histograms are Gaussian fits to the data in logarithmic space. The specific values for GRB 160425A are highlighted with an error bar. **c**, The circumstellar medium density,  $n_{\text{env}}$  (in  $\text{cm}^{-3}$ ), and the electron energy distribution index,  $p$ . The data points are categorized by the GRB class (Short and Long) and the specific model used for the circumstellar medium (ISM or Wind). The central panel is a log-log scatter plot of  $n_{\text{env}}$  against  $p$ . The distributions for each parameter are displayed as histograms on the top ( $p$ ) and right ( $n_{\text{env}}$ ) axes. The data point for GRB 160425A is highlighted with its associated error bar.

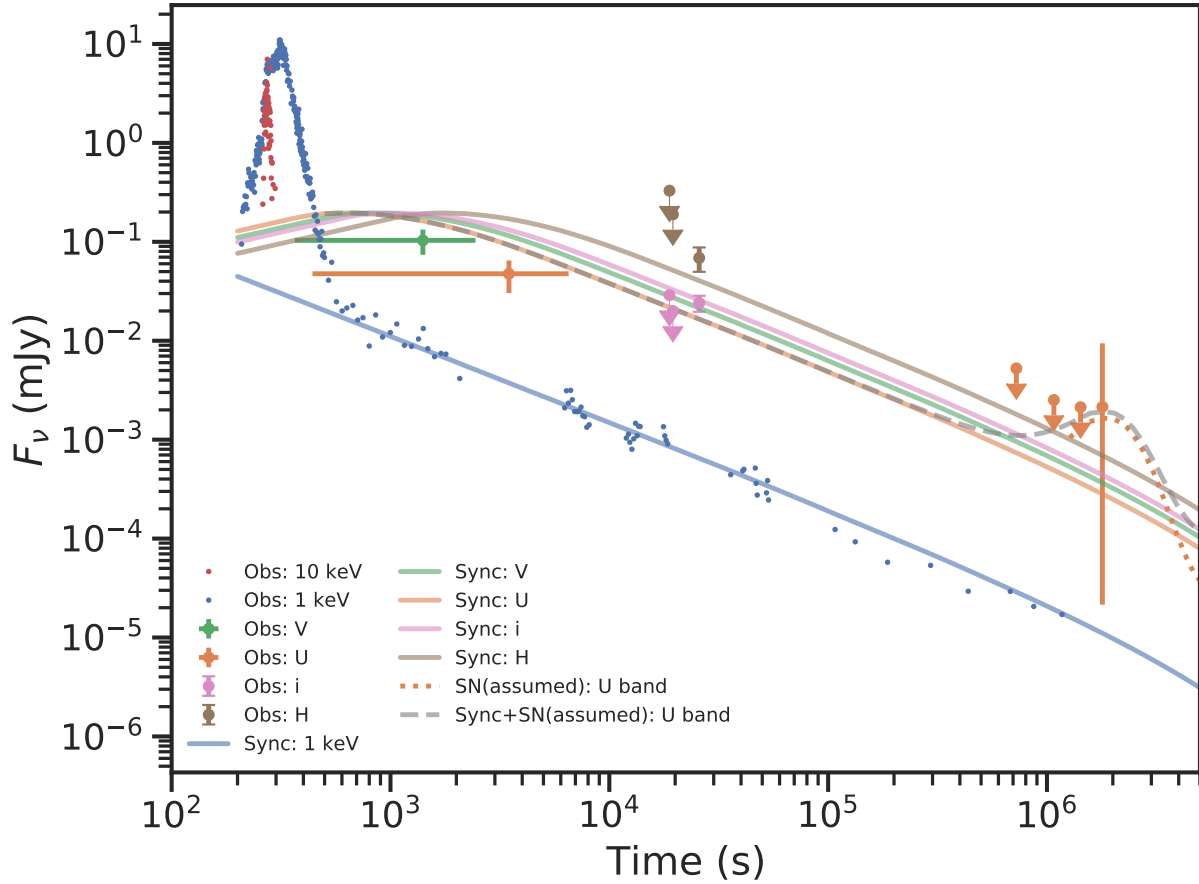


**Figure S4: The multi-wavelength observations and fitting models of GRB 160425A.** Multi-wavelength observations and fitted models of GRB 160425A. The multi-wavelength data (X-ray observed by Swift-BAT and XRT, U and V bands observed by Swift-UVOT, i and H bands observed by GROND and ESO-2.2m MPG) including detections and upper limits, are represented by solid circles and downward arrows, respectively. The best-fit afterglow by the synchrotron emission is represented by dashed curves, the SN component by a dotted curve. Optical data cannot determine the presence of a supernova component. To estimate the maximum luminosity of a potential supernova, we added an orange dotted line (one magnitude fainter than SN 1998bw) and a gray dashed line to represent the hypothetical light curve of the supernova in the U band and the total light curve after incorporating synchrotron radiation, respectively.

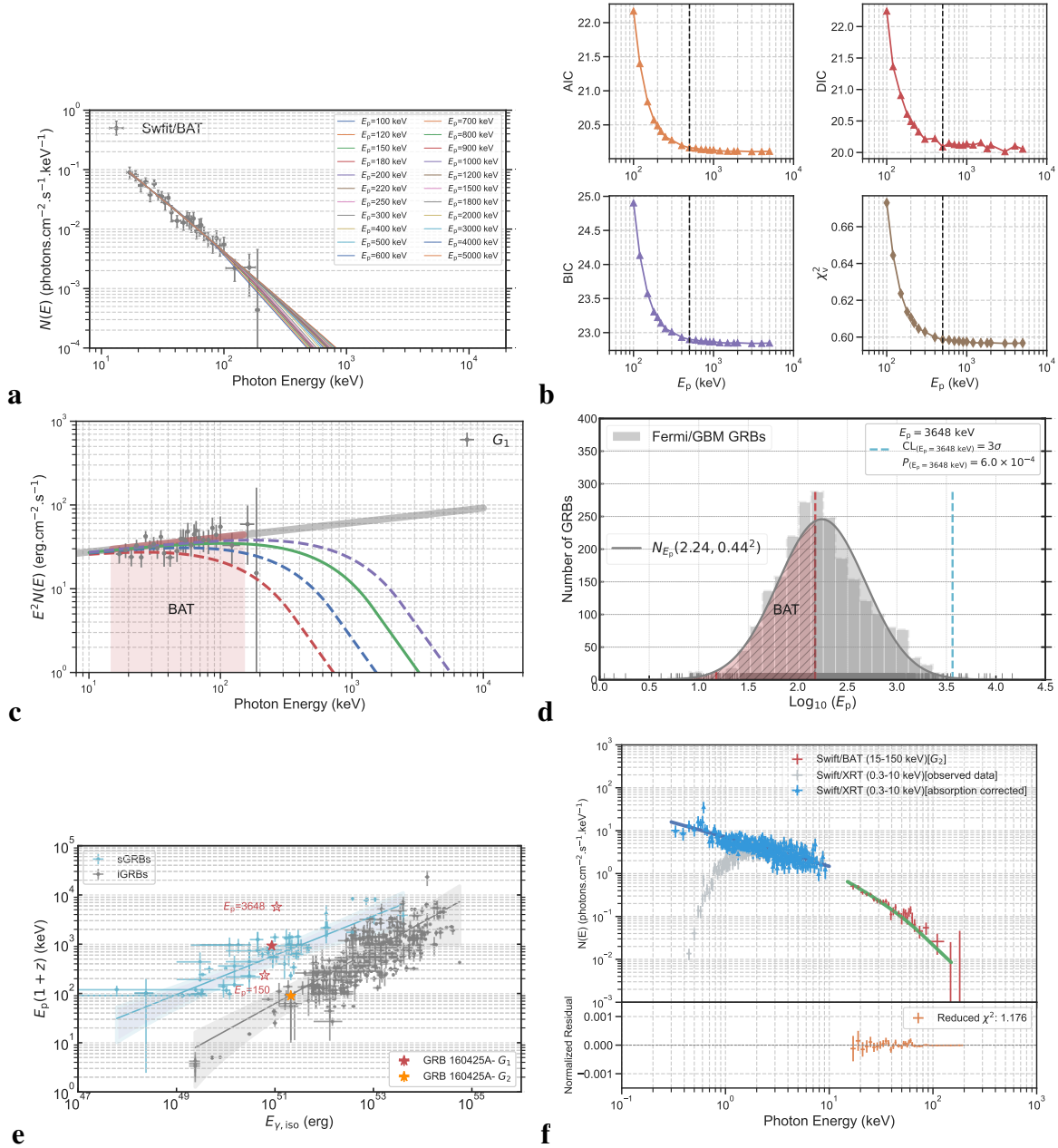


**Figure S5: Spectral fit results of  $G_1$  and  $G_2$ .** **a-c**, The estimated  $E_p$  value of  $G_1$  using spectral shape curvature extrapolation method (76). **a**, The BAT spectra data of  $G_1$  and their best fit using the different Band models with varying  $E_p$  values. **b** The corresponding statistical criteria as a function of  $E_p$ , with the vertical black dashed line indicating the “bending point”. **c**, The corresponding Band function with different  $E_p$  values, indicated by differently colored dashed and solid (corresponding to the “bending point”) lines. **d**, The upper limit of  $E_p$  was estimated using a complete GBM GRB sample. **e**, The Amati  $E_{\gamma, \text{iso}} - E_{p, z}$  correlation diagram for short-duration (cyan data points) and long-duration (gray) as well as their best model fittings (solid lines) and  $2\sigma$  regions (shaded areas). The two individual bursts of GRB are highlighted by red and orange stars, respectively. **f**, The BAT-XRT spectra of  $G_2$  and the best fits using the Band model.

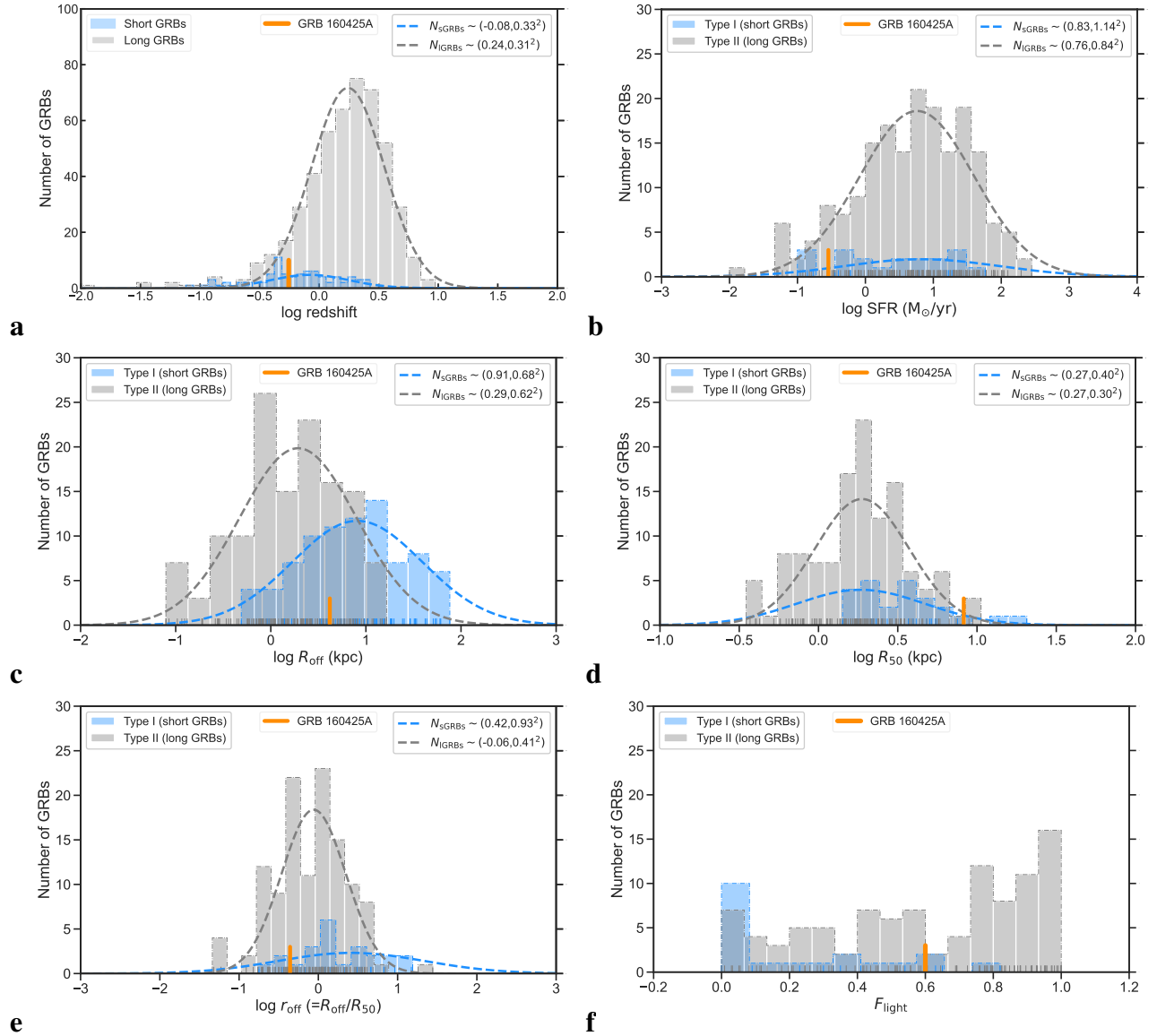


**Figure S6: Host properties of GRB 160425A.** **a**, Distributions of redshift. **b**, Distributions of star formation rate (SFR) of the host galaxies. **c**, Distributions of offset  $R_{off}$ . **d**, Distributions of half light radius  $R_{50}$ . **e**, Distributions of normalized offset ( $r = R_{off}/R_{50}$ ). **f**, Distributions of cumulative light fraction  $F_{light}$ . In all panels (**a-f**), gray and red histograms represent Type I and Type II GRBs, respectively, with the orange vertical cylinder bar indicating the position of GRB 160425A.

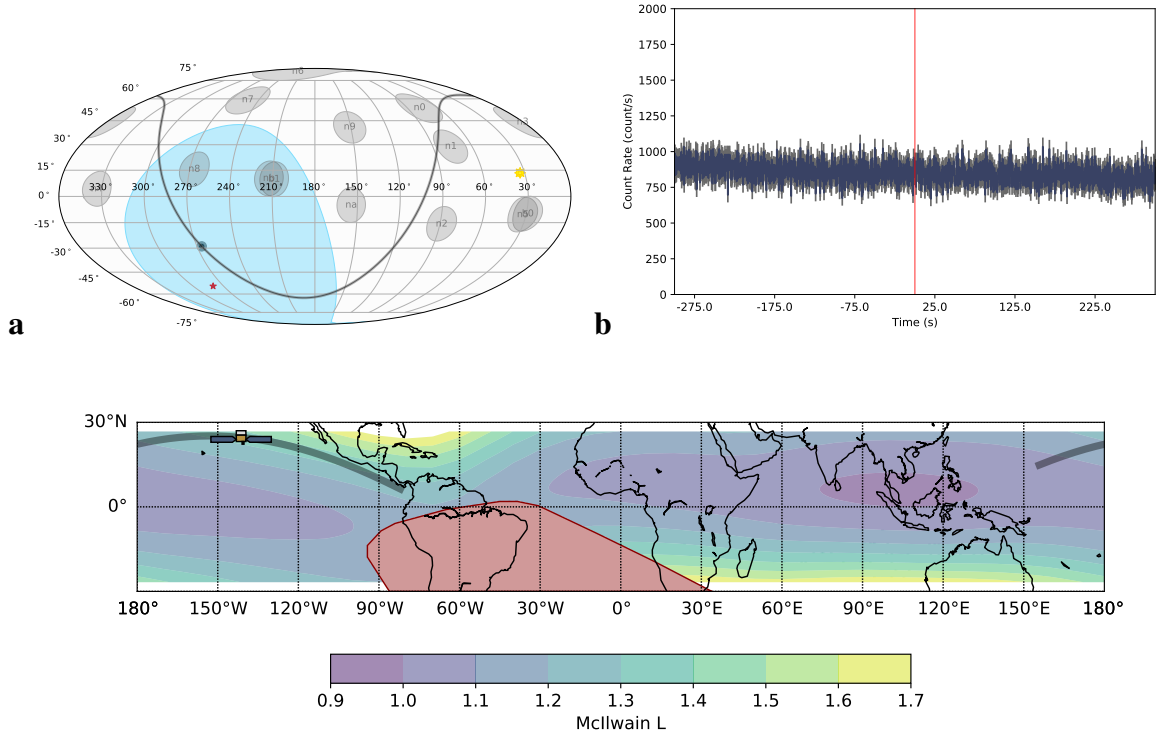


**Figure S7: Untriggered Fermi-GBM signal search and data analysis.** **a**, Position history (POSHIST) data of the Fermi satellite from the Fermi GBM Daily Data for April 25, 2016. The red pentagram marks the location of GRB 160425A, while the blue region represents the Earth. **b**, The all-sky light curve observed by Fermi, shows no clear signal within 5 minutes before and after the trigger time. **c**, Trajectory of the Fermi satellite during the burst of GRB 160425A.

**Table S1:** Spectral fit results of the individual bursts of GRB 160425A.

Burst	$t_1 \sim t_2$ (s)	Normalization ( $\text{ph.s}^{-1}.\text{cm}^{-2}\text{keV}^{-1}$ )	$\alpha$	$E_p$ (keV)	$\beta$	$F_\gamma$ ( $\text{erg.cm}^{-2}.\text{s}^{-1}$ )
$G_1$	-0.20~1.50	$(4.6^{+0.7}_{-0.5}) \times 10^{-3}$	$-1.69^{+0.11}_{-0.09}$	$\gtrsim 500$	-2.3(fixed)	$(5.1 \pm 0.7) \times 10^{-7}$
$G_2$	257.0~308.2	$(2.5^{+0.1}_{-0.1}) \times 10^{-3}$	$-1.17^{+0.02}_{-0.02}$	$57.6^{+2.7}_{-2.7}$	$-2.44^{+0.08}_{-0.08}$	$(4.9 \pm 0.6) \times 10^{-8}$

**Table S2:** Spectral lag properties of GRB 160425A.

Spectral lag ( $\tau[E_1 \sim E_2]$ )	GRB 160425A- $G_1$ (32 ms binning)	GRB 160425A- $G_2$ (256 ms binning)
$\tau[(25-50 \text{ keV}) \sim (15-25 \text{ keV})]$	(38 $\pm$ 39) ms	(1152 $\pm$ 264) ms
$\tau[(50-100 \text{ keV}) \sim (15-25 \text{ keV})]$	(119 $\pm$ 96) ms	(2048 $\pm$ 312) ms
$\tau[(100-350 \text{ keV}) \sim (15-25 \text{ keV})]$	(32 $\pm$ 34) ms	(5862 $\pm$ 154) ms

**Table S3:** Afterglow model fitting parameters for GRB 160425A.

Parameter	Value
$E_{\text{iso}}$ [erg]	$(2.98^{+6.16}_{-1.79}) \times 10^{52}$
$\epsilon_e$	$0.62^{+0.25}_{-0.23}$
$\epsilon_B$	$0.0012^{+0.0056}_{-0.0010}$
$p$	$2.18^{+0.04}_{-0.04}$
$\Gamma_0$	$951^{+566}_{-448}$
$n_0$ [cm $^{-3}$ ]	$0.0016^{+0.020}_{-0.0014}$

**Table S4:** Host-galaxy properties of GRB 160425A in comparison with short-duration and long-duration GRB populations.

Name	SGRBs		LGRBs		GRB 160425A				Classification
	Number	$N_{\text{SGRB}}(\mu, \sigma^2)$	Number	$N_{\text{LGRB}}(\mu, \sigma^2)$	Confidence level	$P_{\text{SGRB}}$	Confidence level	$P_{\text{LGRB}}$	Short vs. Long
$z$	78	$(-0.08, 0.33^2)$	484	$(0.24, 0.31^2)$	$0.54\sigma$	0.29	$1.63\sigma$	0.05	Short
SFR	19	$(0.83, 1.14^2)$	183	$(0.76, 0.84^2)$	$0.93\sigma$	0.18	$1.18\sigma$	0.12	Short
$R_{\text{off}}$	83	$(0.91, 0.68^2)$	132	$(0.29, 0.62^2)$	$0.94\sigma$	0.17	$0.03\sigma$	0.49	Long
$R_{50}$	24	$(0.27, 0.40^2)$	124	$(0.27, 0.30^2)$	$0.32\sigma$	0.63	$0.41\sigma$	0.66	Short
$r_{\text{off}}$	23	$(0.42, 0.93^2)$	118	$(-0.06, 0.41^2)$	$0.62\sigma$	0.27	$0.24\sigma$	0.41	Long
$F_{\text{light}}$	20	Unconstrained	99	Unconstrained	...	...	...	...	Long

**Table S5:** Ultraviolet, Optical and Near-infrared Observations of GRB 160425A.

$T - T_0$ (day)	AB Magnitude	Filter	Telescope	Ref.
$0.005^{+0.001}_{-0.001}$	>18.93	V	<i>Swift</i> -UVOT	(26)
$0.007^{+0.001}_{-0.001}$	>18.36	W2	<i>Swift</i> -UVOT	(26)
$0.007^{+0.002}_{-0.002}$	>18.87	M2	<i>Swift</i> -UVOT	(26)
$0.007^{+0.002}_{-0.002}$	>19.43	U	<i>Swift</i> -UVOT	(26)
$0.007^{+0.002}_{-0.002}$	>20.06	W1	<i>Swift</i> -UVOT	(26)
$0.008^{+0.002}_{-0.002}$	>20.92	B	<i>Swift</i> -UVOT	(26)
$0.012^{+0.004}_{-0.004}$	>19.87	V	<i>Swift</i> -UVOT	(26)
$0.013 \pm 0.008$	$20.16 \pm 0.32$	b	<i>Swift</i> -UVOT	(26)
$0.016 \pm 0.012$	$19.22 \pm 0.31$	v	<i>Swift</i> -UVOT	(26)
$0.017^{+0.005}_{-0.005}$	>19.26	W2	<i>Swift</i> -UVOT	(26)
$0.017^{+0.004}_{-0.004}$	>20.94	B	<i>Swift</i> -UVOT	(26)
$0.018^{+0.005}_{-0.005}$	>20.71	W1	<i>Swift</i> -UVOT	(26)
$0.019^{+0.006}_{-0.006}$	>19.52	U	<i>Swift</i> -UVOT	(26)
$0.019^{+0.006}_{-0.006}$	>20.31	M2	<i>Swift</i> -UVOT	(26)
$0.023^{+0.005}_{-0.005}$	>19.28	V	<i>Swift</i> -UVOT	(26)
$0.025^{+0.002}_{-0.002}$	>20.55	B	<i>Swift</i> -UVOT	(26)
$0.026^{+0.002}_{-0.002}$	>18.55	W2	<i>Swift</i> -UVOT	(26)
$0.026^{+0.001}_{-0.001}$	>18.94	W1	<i>Swift</i> -UVOT	(26)
$0.027^{+0.001}_{-0.001}$	>17.86	U	<i>Swift</i> -UVOT	(26)
$0.028^{+0.001}_{-0.001}$	>17.89	M2	<i>Swift</i> -UVOT	(26)
$0.080^{+0.009}_{-0.010}$	>22.12	W1	<i>Swift</i> -UVOT	(26)
$0.083^{+0.010}_{-0.010}$	>20.10	U	<i>Swift</i> -UVOT	(26)
$0.085^{+0.011}_{-0.009}$	>21.28	B	<i>Swift</i> -UVOT	(26)
$0.087^{+0.001}_{-0.001}$	>21.13	M2	<i>Swift</i> -UVOT	(26)
$0.119^{+0.039}_{-0.040}$	>20.92	W2	<i>Swift</i> -UVOT	(26)
$0.122^{+0.039}_{-0.039}$	>21.07	V	<i>Swift</i> -UVOT	(26)
$0.211^{+0.006}_{-0.009}$	>21.78	B	<i>Swift</i> -UVOT	(26)

**Table S5:** — continued

$T - T_0$ (day)	AB Magnitude	Filter	Telescope	Ref.
0.227	>19.5	I	CTIO-1.3m ANDICAM	(25)
0.227	>16.6	J	CTIO-1.3m ANDICAM	(25)
0.227	>15.7	K	CTIO-1.3m ANDICAM	(25)
0.298±0.008	22.2±0.3	g	ESO-2.2m MPG	(24)
0.298±0.008	21.1±0.2	r	ESO-2.2m MPG	(24)
0.298±0.008	20.7±0.2	i	ESO-2.2m MPG	(24)
0.298±0.008	20.5±0.1	z	ESO-2.2m MPG	(24)
0.298±0.008	19.7±0.2	J	ESO-2.2m MPG	(24)
0.298±0.008	19.4±0.3	H	ESO-2.2m MPG	(24)
0.298±0.008	>18.3	K	ESO-2.2m MPG	(24)
0.377	>19.9	I	CTIO-1.3m ANDICAM	(25)
0.377	>17.9	J	CTIO-1.3m ANDICAM	(25)
0.377	>17.1	K	CTIO-1.3m ANDICAM	(25)
0.04±0.035	20.07±0.26	u	<i>Swift</i> -UVOT	(26)
0.047±0.042	20.24±0.30	w1	<i>Swift</i> -UVOT	(26)
0.082±0.076	>20.8	w2	<i>Swift</i> -UVOT	(26)
0.046±0.041	>19.7	m2	<i>Swift</i> -UVOT	(26)
7.384 <sup>+0.287</sup> <sub>-0.249</sub>	>21.74	W1	<i>Swift</i> -UVOT	(26)
8.389 <sup>+0.293</sup> <sub>-0.314</sub>	>21.75	U	<i>Swift</i> -UVOT	(26)
9.714 <sup>+0.130</sup> <sub>-0.129</sub>	21.74 <sup>+0.37</sup> <sub>-0.29</sub>	W2	<i>Swift</i> -UVOT	(26)
10.613	>20.74	M2	<i>Swift</i> -UVOT	(26)
11.427	>21.74	W1	<i>Swift</i> -UVOT	(26)
12.448 <sup>+0.329</sup> <sub>-0.320</sub>	>22.04	U	<i>Swift</i> -UVOT	(26)
13.543 <sup>+0.430</sup> <sub>-0.417</sub>	21.43 <sup>+0.33</sup> <sub>-0.25</sub>	W2	<i>Swift</i> -UVOT	(26)
14.499 <sup>+0.383</sup> <sub>-0.397</sub>	21.71 <sup>+0.44</sup> <sub>-0.33</sub>	M2	<i>Swift</i> -UVOT	(26)
16.485	>22.08	U	<i>Swift</i> -UVOT	(26)
18.576	21.80 <sup>+0.44</sup> <sub>-0.31</sub>	M2	<i>Swift</i> -UVOT	(26)
20.743	21.89 <sup>+0.36</sup> <sub>-0.27</sub>	U	<i>Swift</i> -UVOT	(26)

**Table S6: Optical and Near-infrared GROND Observations of GRB 160425A.**

$T - T_0$ (day)	AB Magnitude	Filter	Telescope	Ref.
0.218	>20.7	g	GROND	this paper
0.218	>20.9	r	GROND	this paper
0.218	>20.5	i	GROND	this paper
0.218	>20.5	z	GROND	this paper
0.218	>18.4	J	GROND	this paper
0.218	>17.7	H	GROND	this paper
0.218	>17.3	K	GROND	this paper
0.226	>20.9	g	GROND	this paper
0.226	>21.2	r	GROND	this paper
0.226	>20.9	i	GROND	this paper
0.226	>20.8	z	GROND	this paper
0.226	>18.6	J	GROND	this paper
0.226	>18.3	H	GROND	this paper
0.226	>17.4	K	GROND	this paper

**Notes: the same as Table S5 but for GROND observation.**